A HIERARCHIC OPTIMISATION APPROACH TOWARDS LOCKING-FREE SHELL FINITE ELEMENTS

B.A. Izzuddin[1] and Y. Liang[2]

Abstract

A hierarchic optimisation approach is presented for relieving inaccuracies in conforming shell elements arising from locking phenomena. This approach introduces two sets of strain modes: i) objective strain modes, defined in the physical coordinate system, and ii) corrective strain modes, representing conforming strains enhanced with hierarchic strain modes. This leads to two alternative families of element, *objective* and *corrective*, both arising from minimising the difference between objective and corrective strains. Importantly, the proposed approach not only alleviates shear and membrane locking, but it also addresses locking arising from element distortion. The application of the proposed optimisation approach is demonstrated for a 9-noded quadrilateral Lagrangian shell element, where the membrane, bending and transverse shear strains are separately optimised, all within a local co-rotational framework that extends the element application to geometric nonlinear analysis. Several numerical examples, including cases with geometric and material nonlinearity, are finally presented to illustrate the effectiveness of the optimised 9-noded shell element in relieving the various sources of locking.

Keywords: shell element; large displacement analysis; hierarchic optimisation; locking phenomena.

[1] Professor of Computational Structural Mechanics, Department of Civil and Environmental Engineering, Imperial College London, SW7 2AZ, (Corresponding author, b.izzuddin@imperial.ac.uk).
[2] Research student, Department of Civil and Environmental Engineering, Imperial College London SW7 2AZ.

1 INTRODUCTION

Ever since the emergence of the displacement-based finite element method, a most serious problem that has influenced its application in linear and nonlinear structural analysis has been related to the locking phenomenon, in which the element exhibits an over-stiff response resulting from its inability to correctly model lower-order modes. The significance of this phenomenon is determined by several factors, including the type of structural analysis problem, the theory underlying the associated mathematical model, as well as the element shape and order. Early forms of locking were observed in the modelling of plate bending problems using the Reissner-Mindlin hypothesis [1], where the inability of a mesh of conforming elements to bend without inducing transverse shear strains leads to deteriorating performance as the plate thickness is reduced, a phenomenon referred to as shear locking. Other forms of locking can also arise with conforming elements, such as membrane locking when using curved shell elements, and distortion locking when employing isoparametric mapping with irregular element shapes.

Whilst locking phenomena may be viewed from several different perspectives depending on the context of element application, a common feature is the degradation in the approximation of various strains over the element domain, principally due to polluting higher-order strains. Numerous research efforts have been devoted to addressing this issue over the past few decades, which can be grouped under distinct strands, as briefly reviewed in the following.

Uniform reduced integration [2-4] addresses element locking by filtering out higher-order stiffness terms via the employment of a reduced number of integration points, which in turn suffers from rank deficiency leading to spurious mechanisms. Selective reduced integration [5-8] improves the shear locking performance of Reissner-Mindlin plate bending elements by employing reduced integration for only the transverse shear strain terms while utilising full integration on the remaining terms, which effectively addresses the rank deficiency issue. However, such a technique is restricted to plates with uncoupled flexural and transverse shear actions, and accordingly it cannot be employed for modelling the nonlinear elasto-plastic material response.

There are a few enhanced displacement methods in the literature [9-11], which generally eliminate shear locking by introducing extra displacement parameters at the expense of enlarging the stiffness matrix. On the other hand, the enhanced assumed strain method [12,13] addresses locking by enriching the element with enhanced strain fields, where the enhanced strain parameters are condensed out using the Hu-Washizu variational principle. Later, Korelc and Wriggers [14] used a Taylor series expansion of strains with respect to natural coordinates for improving the behaviour of distorted elements and relieving the coupling of enhanced modes. Another group of assumed strain methods eliminates polluting higher-order strains by sampling and interpolating strain components at selected locations [15-20]. The components to be sampled, the locations of the sampling points, and the interpolation functions vary in the literature. The Mixed Interpolation of Tensorial Components (MITC) family of elements [20-23], as a specific group of the two-level approximation method, performs sampling and mapping in a covariant coordinate system. Nevertheless, the performance of these strain mapping elements relies strongly on the locations of sampled strains for the assumed interpolation, which can lead to degradation of accuracy for irregular element shapes. To extend the ability of the elements based on the strain mapping method to highly irregular element shapes, Wisniewski and Panasz [24] used corrected shape functions in the element formulation, which addresses the sensitivity to mesh distortions, though nonlinear equations must be solved for determining the additional parameters describing the element distortion.

In this work, an optimisation approach is proposed for nonlinear shell finite elements which not only alleviates shear and membrane locking, but also addresses locking arising from element distortion. The concept behind this approach was originally proposed by the first author [25] and is elaborated and enhanced in the present paper. This approach can be regarded as an assumed strain method, but it has three distinct features. Firstly, it introduces the notion of *objective* strain modes, defined as polynomial functions in terms of physical Cartesian element coordinates, which act as the target strain modes for *corrective* strain modes that represent conforming strains enhanced with hierarchic strain modes. The objective and corrective strain parameters are obtained from mathematical optimisation, and

this leads to two alternative families of element, denoted by acronym keys O and C, in which assumed strains based respectively on the objective or corrective strain fields are directly mapped at the element level to the conforming strains. Secondly, the hierarchic correcting strain modes are established from hierarchic displacement modes defined in the natural coordinate system, where modes up to any hierarchic order *m* can be considered in the element optimisation process for both the O and C element families. Importantly, these hierarchic strain modes are used solely for the purpose of optimisation of the objective and corrective strain fields, and as such do not influence the number of element degrees of freedom (DOF). Thirdly, geometric nonlinearity is considered within a co-rotational framework [26], with the Reissner-Mindlin hypothesis employed for the local shell element response, which enables optimal mapping between objective/corrective and conforming strains to be established for an element from the solution of a linear system of equations. In this respect, the optimal mapping for individual elements need only be established once, at the start of incremental nonlinear analysis, and further computational benefits arise from uncoupled mappings of the planar, bending and transverse shear strains, which can be applied in the proposed approach even to elements with local geometric nonlinearity.

Noting the above distinct features, the resulting families of hierarchically optimised elements are denoted by acronyms H*m*O*n* and H*m*C*n*, corresponding respectively to the objective (O) and corrective (C) assumed strain families, where *m* is the order of hierarchic displacement fields used for defining the hierarchic correcting strain modes, and *n* refers to the number of element nodes. Thus for example, H3O9 refers to a quadrilateral 9-noded Reissner-Mindlin shell element, with quadratic Lagrangian shape functions and cubic hierarchic displacement modes ($m = 3$) for the hierarchic correcting strains, and with the assumed strains based on the objective (O) strain modes.

The paper proceeds with presenting the general formulation of the proposed hierarchic optimisation approach. The application of this approach to the local formulation of a quadrilateral 9-noded Reissner-Mindlin shell element is then elaborated, leading to the two aforementioned families of optimised elements H*m*O9 and H*m*C9. To facilitate direct comparisons against previous high performing elements, two local MITC9 formulations

[22,24] are implemented in the same code alongside the proposed H*m*O9 and H*m*C9 elements, where minor adjustments are presented in Appendix A focused on ensuring similar underlying kinematic assumptions in the local system. This is followed by outlining the incorporation of the various local 9-noded element formulations within a co-rotational framework, based on the bisector definition of the local system [26], so as to enable the modelling of geometric nonlinearity. Several numerical examples are finally provided to demonstrate the effectiveness and relative accuracy of the proposed optimised 9-noded element formulations compared to the 9-noded conforming element [27], 9-noded Reissner-Mindlin elements adopting the MITC9 strain-mapping method, and other previously developed shell element formulations.

2 HIERARCHIC OPTIMISATION APPROACH

The locking phenomena in conforming finite elements is generally characterised by the degraded approximation of various strains over the element domain, principally owing to polluting higher-order strains. To illustrate this point and introduce the proposed concept of hierarchic optimisation, consider the 1D Euler-Bernoulli beam-column element depicted in Figure 1, where 3 parameters $(\theta_1, \theta_2, \Delta)$ define the element deformed configuration in a local co-rotational system. For this basic element, linear and cubic polynomial shape function can be employed for the local axial and transverse displacement fields:

$$u(x) = \left(\frac{x}{L}\right)\Delta, \quad v(x) = \left(x - \frac{2x^2}{L} + \frac{x^3}{L^2}\right)\theta_1 + \left(-\frac{x^2}{L} + \frac{x^3}{L^2}\right)\theta_2 \tag{1}$$

Although the co-rotational approach [26] allows a linear strain-displacement relationship to be employed in the local system for the generalised curvature and centroidal axial strains, κ and ε_c respectively, the element achieves improved approximation with a coarser mesh if a quadratic relationship is used for ε_c as follows:

$$\begin{Bmatrix} \kappa \\ \varepsilon_c \end{Bmatrix} = \begin{Bmatrix} \dfrac{\mathrm{d}^2 v}{\mathrm{d}x^2} \\ \dfrac{\mathrm{d}u}{\mathrm{d}x} + \dfrac{1}{2}\left(\dfrac{\mathrm{d}v}{\mathrm{d}x}\right)^2 \end{Bmatrix} \tag{2}$$

Focusing on the approximation of $\varepsilon_c(x)$ according to the compatibility conditions in (2), it is evident considering (1) that the conforming $\varepsilon_c(x)$ is constant over the element when it is subjected to pure axial deformation with $u(x) \neq 0$ and $v(x) = 0$. However, in the presence of bending deformations with $v(x) \neq 0$, the approximation of the conforming $\varepsilon_c(x)$ is no longer the constant function afforded by the element but is instead polluted by a 4th order polynomial function of x arising from the $(\mathrm{d}v/\mathrm{d}x)^2$ term. Accordingly, the approximation of the conforming $\varepsilon_c(x)$ is adversely affected by $v(x)$, which leads to membrane locking since the element cannot bend without inducing $\varepsilon_c(x)$, regardless of the value of the axial displacement parameter Δ. In this respect, the recovery of the original constant approximation of $\varepsilon_c(x)$ requires $u(x)$ to be a 5th order function, with the terms above 2nd order dependent on (θ_1, θ_2). An alternative approach, which is more generally applicable to different types of element, would be to consider hierarchic strain corrections $\varepsilon_{ch}(x)$ obtained from a hierarchic axial displacement field $u_h(x)$, which satisfies the nodal displacement boundary conditions, such as the following 5th order field:

$$\varepsilon_{ch} = \frac{\mathrm{d}u_h}{\mathrm{d}x},\ u_h(x) = x(x-L)\delta_1 + x^2(x-L)\delta_2 + x^3(x-L)\delta_3 + x^4(x-L)\delta_4 \tag{3}$$

and then optimise the corrected strain field towards the objective strain field, which is constant in the current illustration for the 1D element:

$$\varepsilon_c + \varepsilon_{ch} \rightarrow \varepsilon_{co}, \quad \varepsilon_{co} = \text{constant} \tag{4}$$

Extending the above illustrated concept to 2D shell finite elements, the proposed optimisation approach is based on employing hierarchic strain parameters, associated with hierarchic higher-order shape functions beyond those used in the conforming element formulation, such that the combination of the conforming strains $\boldsymbol{\varepsilon}$ and the hierarchic correcting strains $\boldsymbol{\varepsilon}_h$, denoted as the *corrective* strains ($\boldsymbol{\varepsilon} + \boldsymbol{\varepsilon}_h$), offers a close approximation of the strain distribution $\boldsymbol{\varepsilon}_o$ afforded by the original element DOFs in terms of physical Cartesian element coordinates. In this respect, the *objective* strain vector $\boldsymbol{\varepsilon}_o$ combines contributions from various strain-inducing modes $\boldsymbol{\Psi}_o$ associated with the strain field under consideration, where the number of such modes depends on the associated DOFs of the conforming element. Accordingly, $\boldsymbol{\varepsilon}$ is enhanced with $\boldsymbol{\varepsilon}_h$ towards $\boldsymbol{\varepsilon}_o$:

$$\boldsymbol{\varepsilon} + \boldsymbol{\varepsilon}_h \rightarrow \boldsymbol{\varepsilon}_o, \quad \boldsymbol{\varepsilon}_h = \boldsymbol{\Psi}_h \boldsymbol{\alpha}_h, \quad \boldsymbol{\varepsilon}_o = \boldsymbol{\Psi}_o \boldsymbol{\alpha}_o \tag{5}$$

where $\boldsymbol{\Psi}_h$ and $\boldsymbol{\Psi}_o$ represent the hierarchic and objective strain modes, respectively, while $\boldsymbol{\alpha}_h$ and $\boldsymbol{\alpha}_o$ are the respective associated strain parameters.

The employment of mathematical optimisation leads to a minimisation of the difference between the corrective strains ($\boldsymbol{\varepsilon}$ + $\boldsymbol{\varepsilon}_h$) and the objective strains $\boldsymbol{\varepsilon}_o$. Considering the target of optimisation to be a functional integrating the square of this difference over the element domain, the strain parameters are easily obtained for a given set of conforming strains $\boldsymbol{\varepsilon}$ from the solution of the following linear system of equations:

$$\left(\int_{\Omega^e} \left[\begin{array}{c|c} \boldsymbol{\Psi}_h^{\mathrm{T}} \boldsymbol{\Psi}_h & -\boldsymbol{\Psi}_h^{\mathrm{T}} \boldsymbol{\Psi}_o \\ \hline -\boldsymbol{\Psi}_o^{\mathrm{T}} \boldsymbol{\Psi}_h & \boldsymbol{\Psi}_o^{\mathrm{T}} \boldsymbol{\Psi}_o \end{array} \right] \mathrm{d}\Omega^e \right) \left\{ \begin{array}{c} \boldsymbol{\alpha}_h \\ \hline \boldsymbol{\alpha}_o \end{array} \right\} = \int_{\Omega^e} \left[\begin{array}{c} -\boldsymbol{\Psi}_h^{\mathrm{T}} \\ \hline \boldsymbol{\Psi}_o^{\mathrm{T}} \end{array} \right] \boldsymbol{\varepsilon} \, \mathrm{d}\Omega^e \tag{6}$$

in which Ω^e is the element domain. The proposed approach can also accommodate other quadratic functionals based on the difference between the corrective and objective strains [28], leading to alternative but equally straightforward linear systems of equations for determining the strain parameters.

The determination of the strain parameters $\boldsymbol{\alpha}_h$ and $\boldsymbol{\alpha}_o$ from the conforming strains without reference to the element displacement preserves the computational efficiency, particularly in the presence of nonlinear strain-displacement relationships, and the conforming strains are accordingly enhanced with hierarchic higher-order strains towards the objective strains. The enhanced strains can be expressed in either the corrective or the objective form, where the difference between the two alternative approaches reduces with either the hierarchic order or mesh refinement:

$$\tilde{\boldsymbol{\varepsilon}} = \boldsymbol{\varepsilon} + \boldsymbol{\Psi}_h \boldsymbol{\alpha}_h \quad \text{(Corrective)} \tag{7}$$

$$\hat{\boldsymbol{\varepsilon}} = \boldsymbol{\Psi}_{\mathrm{o}} \boldsymbol{\alpha}_{\mathrm{o}} \quad \text{(Objective)} \tag{8}$$

Unlike previous enhanced assumed strain approaches [12-14], the proposed approach leads to two variant element families, depending on whether the corrective (C) or objective (O) fields are adopted for the assumed strains. Furthermore, while the corrective strain field $\boldsymbol{\varepsilon}_h$ resembles the enhanced assumed strain in previous approaches, its approximation order is not capped to a prescribed distribution but can attain any hierarchic order *m*. On the other

hand, the additionally introduced objective strain field $\boldsymbol{\varepsilon}_o$ is similar conceptually to an assumed strain field based on sampling at selected locations [16-23], but it is different in two ways: i) it utilises a polynomial basis in physical Cartesian coordinates which effectively addresses distortion locking in isoparametric element formulations with irregular element configuration, and ii) it is recovered via an optimisation process that considers the conforming strains $\boldsymbol{\varepsilon}$ over the whole element domain rather than at a fixed number of sampling points.

For isoparametric elements, the integration is most effectively carried out with Gaussian quadrature, and hence the solution for $\boldsymbol{\alpha}_h$ and $\boldsymbol{\alpha}_o$ can be related to the strains $\boldsymbol{\varepsilon}_{(i)}$ at the Gauss points as follows:

$$\boldsymbol{\alpha}_h = \boldsymbol{\Gamma}_h \begin{Bmatrix} \boldsymbol{\varepsilon}_{(1)} \\ \vdots \\ \boldsymbol{\varepsilon}_{(i)} \\ \vdots \end{Bmatrix}, \quad \boldsymbol{\alpha}_o = \boldsymbol{\Gamma}_o \begin{Bmatrix} \boldsymbol{\varepsilon}_{(1)} \\ \vdots \\ \boldsymbol{\varepsilon}_{(i)} \\ \vdots \end{Bmatrix} \tag{9}$$

in which the subscript (i) represents the Gauss point number.

Therefore, the enhanced strains at the Gauss points can be determined as follows, depending on the alternative approach:

$$\begin{Bmatrix} \tilde{\boldsymbol{\varepsilon}}_{(1)} \\ \vdots \\ \tilde{\boldsymbol{\varepsilon}}_{(i)} \\ \vdots \end{Bmatrix} = \tilde{\mathbf{T}} \begin{Bmatrix} \boldsymbol{\varepsilon}_{(1)} \\ \vdots \\ \boldsymbol{\varepsilon}_{(i)} \\ \vdots \end{Bmatrix}, \quad \tilde{\mathbf{T}} = \mathbf{I} + \begin{bmatrix} \boldsymbol{\Psi}_{h(1)} \\ \vdots \\ \boldsymbol{\Psi}_{h(i)} \\ \vdots \end{bmatrix} \boldsymbol{\Gamma}_h \quad \text{(Corrective)} \tag{10}$$

$$\begin{Bmatrix} \hat{\boldsymbol{\varepsilon}}_{(1)} \\ \vdots \\ \hat{\boldsymbol{\varepsilon}}_{(i)} \\ \vdots \end{Bmatrix} = \hat{\mathbf{T}} \begin{Bmatrix} \boldsymbol{\varepsilon}_{(1)} \\ \vdots \\ \boldsymbol{\varepsilon}_{(i)} \\ \vdots \end{Bmatrix}, \quad \hat{\mathbf{T}} = \begin{bmatrix} \boldsymbol{\Psi}_{o(1)} \\ \vdots \\ \boldsymbol{\Psi}_{o(i)} \\ \vdots \end{bmatrix} \boldsymbol{\Gamma}_o \quad \text{(Objective)} \tag{11}$$

in which $\tilde{\mathbf{T}}$ and $\hat{\mathbf{T}}$ are the transformation matrices from conforming strains to corrective strains and objective strains, respectively, at the Gauss points.

Clearly, the above alternative approaches correspond to an assumed strain formulation, though the assumed strains are the result of optimisation towards a specific target strain

distribution afforded by the original conforming DOFs, as demonstrated in the application to a 9-noded curved shell element presented in the next section. For geometrically linear elements, which employ a first-order strain-displacement relationship, the assumed strains $\tilde{\boldsymbol{\varepsilon}}$ or $\hat{\boldsymbol{\varepsilon}}$ can be directly related to the original DOFs via a respective strain operator $\tilde{\mathbf{B}}$ or $\hat{\mathbf{B}}$, since $\boldsymbol{\varepsilon}$ is readily related to such DOFs through the conventional conforming $\mathbf{B}$ matrix. For geometrically nonlinear elements, however, it is more effective to determine the conforming strains and then transform these to assumed strains according to (10) or (11).

In using Gaussian quadrature to integrate and subsequently solve (6), a minimum number of sampling points is required, depending on the order and number of hierarchic terms considered, which can be more than what is typically required for the conforming element. Although this implies that the conforming strains need to be sampled at more points than in the typical element, it is still possible to determine the assumed strains at a reduced number of points through an additional mapping process beyond the results of (10) or (11). This refinement, however, is not considered herein.

3 LOCAL FORMULATION OF OPTIMISED 9-NODED SHELL ELEMENT

The proposed optimisation approach is applied to relieve membrane, shear and distortion locking in a local formulation of a previously developed 9-noded conforming quadrilateral Reissner-Mindlin shell element [27], which is formulated in a co-rotational framework [26] for large displacement analysis. The local kinematics of the conforming element are first presented, and the application of the proposed optimisation approach is detailed, leading to the formulation of the two element families H*m*O9 and H*m*C9, corresponding respectively to the objective and corrective variants of the 9-noded shell element.

3.1 Local kinematics of 9-noded conforming shell element

Figure 2 presents three different coordinate systems for the 9-noded Lagrangian shell element undergoing large displacements, where (X, Y, Z) is the global Cartesian coordinate system, (x, y, z) is the local Cartesian coordinate system, and (ξ, η) is the 2D natural coordinate system. As shown in Figure 3, the $\left(\mathbf{c}_{\mathrm{x}}, \mathbf{c}_{\mathrm{y}}, \mathbf{c}_{\mathrm{z}}\right)$ triad describing the orientation of

the local element co-rotational system is defined such that the *x*- and *y*-axes always coincide with the bisectors of the diagonal vectors generated from the four corner nodes, while the *z*-axis is orthogonal to the *xy* plane [26]. With the employment of the co-rotational system, the large-displacement small-strain problem in the global system is transformed in the local system to a small-displacement small-strain problem, and the focus of large-displacement modelling is shifted from the continuum to the discrete level [26].

The local element shape and displacement fields are interpolated with quadratic Lagrangian shape functions in terms of natural coordinates (ξ, η):

$$\mathbf{x} = \begin{Bmatrix} x \\ y \\ z \end{Bmatrix} = \sum_{i=1}^{9} N_i(\xi, \eta)\mathbf{x}_i \tag{12}$$

$$\mathbf{t} = \begin{Bmatrix} u \\ v \\ w \end{Bmatrix} = \sum_{i=1}^{9} N_i(\xi, \eta)\mathbf{t}_i, \quad \bar{\mathbf{r}} = \begin{Bmatrix} \theta_x \\ \theta_y \end{Bmatrix} = \sum_{i=1}^{9} N_i(\xi, \eta)\bar{\mathbf{r}}_i \tag{13}$$

in which $\mathbf{x}_i = \langle x_i \;\; y_i \;\; z_i \rangle^{\mathrm{T}}$ are local nodal coordinates of node *i* in the initial configuration; $\mathbf{t}_i = \langle u_i \;\; v_i \;\; w_i \rangle^{\mathrm{T}}$ are local nodal translations of node *i*; and $\bar{\mathbf{r}}_i = \langle \theta_{ix} \;\; \theta_{iy} \rangle^{\mathrm{T}}$ represents the local nodal rotations of node *i* (θ_{ix} is the nodal rotation about y-axis and θ_{iy} is the nodal rotation about the negative x-axis).

The shape functions are of the Lagrangian form:

$$N_i(\xi, \eta) = \frac{(\xi - \xi_i')(\xi - \xi_i'')}{(\xi_i - \xi_i')(\xi_i - \xi_i'')} \cdot \frac{(\eta - \eta_i')(\eta - \eta_i'')}{(\eta_i - \eta_i')(\eta_i - \eta_i'')} \quad (i = 1 \to 9) \tag{14}$$

where: (ξ_i, η_i) represents the natural coordinates of node *i*; $(\xi_i \neq \xi_i' \neq \xi_i'') = -1,\ 0,\ 1$ and $(\eta_i \neq \eta_i' \neq \eta_i'') = -1,\ 0,\ 1$.

The element strain state is fully determined by membrane strains $\boldsymbol{\varepsilon}^m$, bending generalised strains $\boldsymbol{\varepsilon}^b$, and transverse shear strains $\boldsymbol{\varepsilon}^s$. Local geometric nonlinearity is addressed through quadratic approximation of the membrane strains, while the influence of large displacements is accounted for through transformations between the local co-rotational system and the global system [27]. Accordingly, various generalised strains are obtained as follows:

$$\boldsymbol{\varepsilon}^m = \begin{Bmatrix} \varepsilon_x \\ \varepsilon_y \\ \gamma_{xy} \end{Bmatrix} = \begin{Bmatrix} \dfrac{\partial u}{\partial x} \\ \dfrac{\partial v}{\partial y} \\ \dfrac{\partial u}{\partial y} + \dfrac{\partial v}{\partial x} \end{Bmatrix} + \begin{Bmatrix} \dfrac{1}{2}\left(\dfrac{\partial z}{\partial x} + \dfrac{\partial w}{\partial x}\right)^2 - \dfrac{1}{2}\left(\dfrac{\partial z}{\partial x}\right)^2 \\ \dfrac{1}{2}\left(\dfrac{\partial z}{\partial y} + \dfrac{\partial w}{\partial y}\right)^2 - \dfrac{1}{2}\left(\dfrac{\partial z}{\partial y}\right)^2 \\ \left(\dfrac{\partial z}{\partial x} + \dfrac{\partial w}{\partial x}\right)\left(\dfrac{\partial z}{\partial y} + \dfrac{\partial w}{\partial y}\right) - \left(\dfrac{\partial z}{\partial x}\right)\left(\dfrac{\partial z}{\partial y}\right) \end{Bmatrix} \tag{15a}$$

$$\boldsymbol{\varepsilon}^b = \begin{Bmatrix} \kappa_x \\ \kappa_y \\ \kappa_{xy} \end{Bmatrix} = \begin{Bmatrix} \dfrac{\partial \theta_x}{\partial x} \\ \dfrac{\partial \theta_y}{\partial y} \\ \dfrac{\partial \theta_x}{\partial y} + \dfrac{\partial \theta_y}{\partial x} \end{Bmatrix} \tag{15b}$$

$$\boldsymbol{\varepsilon}^s = \begin{Bmatrix} \gamma_{xz} \\ \gamma_{yz} \end{Bmatrix} = \begin{Bmatrix} \theta_x + \dfrac{\partial w}{\partial x} \\ \theta_y + \dfrac{\partial w}{\partial y} \end{Bmatrix} \tag{15c}$$

3.2 Objective strain modes

A common feature of the locking phenomena is the inability of the element to generate some of the lower-order strain modes over the element domain, principally due to polluting higher-order strains induced by the underlying element kinematic assumptions, the strain-displacement relationship, and the irregular element shape. The hierarchic optimisation approach aims at restoring the lower-order strain fields by enhancing the conforming strains towards a set of prescribed objective strain modes which are of lower-order in terms of physical Cartesian coordinates and as afforded by the element DOFs. It is important to note that the objective strain modes are defined as polynomial functions of real physical coordinates rather than natural coordinates, so that the element is less sensitive to distortion. In the following, a complete set of lower-order objective strain modes specific to the 9-noded shell element is presented, based on which the hierarchic optimisation approach is performed separately for the generalised membrane, bending and transverse shear strains to eliminate locking.

The planar displacements (u, v) for a 9-noded shell element can generate three rigid body modes and fifteen membrane strain-inducing modes. Therefore, fifteen low-order objective planar modes can be afforded by this element, for which the corresponding membrane strains are expressed as:

$$\boldsymbol{\Psi}_o^m = \begin{bmatrix} \dfrac{\partial}{\partial x} & 0 \\ 0 & \dfrac{\partial}{\partial y} \\ \dfrac{\partial}{\partial y} & \dfrac{\partial}{\partial x} \end{bmatrix} \boldsymbol{\Phi}_o^m \tag{16}$$

where $\boldsymbol{\Phi}_o^m$ are objective planar strain-inducing modes from Pascal's triangle, given by:

$$\boldsymbol{\Phi}_o^m = \left[\begin{array}{ccc:c:c} x & y & 0 & \boldsymbol{\Phi}_o^2 & \mathbf{0} \\ 0 & x & y & \mathbf{0} & \boldsymbol{\Phi}_o^2 \end{array}\right], \quad \boldsymbol{\Phi}_o^2 = \left\langle x^2 \;\; xy \;\; y^2 \;\; x^2y \;\; xy^2 \;\; x^2y^2 \right\rangle \tag{17}$$

The transverse displacement field (w) for the 9-noded shell element can generate one rigid body mode and eight transverse shear strain modes. Therefore, eight low-order objective transverse modes can be afforded by this element, for which the corresponding transverse shear strains are expressed as:

$$\boldsymbol{\Psi}_o^{s,z} = \begin{Bmatrix} \dfrac{\partial}{\partial x} \\ \dfrac{\partial}{\partial y} \end{Bmatrix} \boldsymbol{\Phi}_o^{s,z} \tag{18}$$

where $\boldsymbol{\Phi}_o^{s,z}$ are objective transverse strain-inducing modes given by:

$$\boldsymbol{\Phi}_o^{s,z} = \left\langle x \;\; y \;\; x^2 \;\; xy \;\; y^2 \;\; x^2y \;\; xy^2 \;\; x^2y^2 \right\rangle \tag{19}$$

The rotational fields (θ_x, θ_y) of a 9-noded element can generate fifteen curvature-inducing modes, with the objective curvature modes being the same as the above membrane strain modes:

$$\boldsymbol{\Psi}_o^b = \boldsymbol{\Psi}_o^m \tag{20}$$

With four rigid body modes already accounted for in relation to the planar and transverse displacement field, the remaining two rigid body modes are generated by combining the two

constant rotation modes with a linear distribution of the transverse displacement. This leaves one rotational mode that generates no curvatures but a linear transverse shear strain mode $\boldsymbol{\Psi}_o^{s,\theta} = \langle -y, x \rangle^{\mathrm{T}}$, which is not included in (18). Therefore, a complete objective set of transverse shear strain modes is given by:

$$\boldsymbol{\Psi}_o^s = \left[\boldsymbol{\Psi}_o^{s,z} \,\vdots\, \boldsymbol{\Psi}_o^{s,\theta} \right] \tag{21}$$

Accordingly, there are in total 39 objective strain modes for the 9-noded shell element (15 membrane $\boldsymbol{\Psi}_o^m$, 15 curvature $\boldsymbol{\Psi}_o^b$, and 9 transverse shear $\boldsymbol{\Psi}_o^s$), which ensure the correct rank of the element stiffness matrix. In the following, the hierarchic optimisation approach is employed to address shear, membrane and distortion locking in the local element formulation with the employment of the above objective strain modes $\boldsymbol{\Psi}_o^m$, $\boldsymbol{\Psi}_o^b$, and $\boldsymbol{\Psi}_o^s$.

3.3 Shear Locking

Consideration is first given to the transverse shear strains in (15c). It is clear that the conforming element cannot bend in any arbitrary mode (θ_x, θ_y), as allowed by its rotational DOFs, without polluting $(\gamma_{xz}, \gamma_{yz})$ with second-order terms. Although the transverse displacement field (w) via the associated translational DOFs, offers an effective first-order approximation of $(\gamma_{xz}, \gamma_{yz})$, the polluting terms from (θ_x, θ_y) can lead to a significant overestimation of the transverse shear strain energy, hence causing shear locking. These polluting terms can be filtered out by introducing hierarchic correcting strain modes, with the aim of achieving the first-order approximation of $(\gamma_{xz}, \gamma_{yz})$ afforded by the element, as given by the objective shear strain modes $\boldsymbol{\Psi}_o^s$.

The hierarchic transverse displacement modes, which are used to establish the hierarchic strains, are defined as polynomial functions of natural coordinates (ξ, η). The hierarchic optimisation approach can utilise hierarchic modes up to any order, where complete cubic and quartic displacement modes are considered below:

$$w_h(\xi, \eta) = \boldsymbol{\Phi}_h^s \boldsymbol{\alpha}_h^s, \quad \boldsymbol{\Phi}_h^s = \left\langle \boldsymbol{\Phi}_h^3 \,\vdots\, \boldsymbol{\Phi}_h^4 \,\vdots\, \cdots \right\rangle \tag{22}$$

$$\boldsymbol{\Phi}_h^3 = \left\langle \chi(\xi)\ \chi(\eta)\ \eta\chi(\xi)\ \xi\chi(\eta)\ \eta^2\chi(\xi)\ \xi^2\chi(\eta)\ \chi(\xi)\chi(\eta) \right\rangle \tag{23}$$

$$\boldsymbol{\Phi}_h^4 = \left\langle \omega(\xi)\ \omega(\eta)\ \eta\omega(\xi)\ \xi\omega(\eta)\ \eta^2\omega(\xi)\ \xi^2\omega(\eta)\ \eta^3\omega(\xi)\ \xi^3\omega(\eta)\ \omega(\xi)\omega(\eta) \right\rangle \tag{24}$$

with:

$$\chi(\delta) = \delta(\delta^2 - 1), \quad \omega(\delta) = \delta^2(\delta^2 - 1), \quad \delta = \xi, \eta \tag{25}$$

The corresponding hierarchic shear strains are therefore obtained from:

$$\boldsymbol{\varepsilon}_h^s = \begin{Bmatrix} \gamma_{xzh} \\ \\ \gamma_{yzh} \end{Bmatrix} = \begin{Bmatrix} \dfrac{\partial}{\partial x} \\ \\ \dfrac{\partial}{\partial y} \end{Bmatrix} w_h = \boldsymbol{\Psi}_h^s \boldsymbol{\alpha}_h^s, \quad \boldsymbol{\Psi}_h^s = \begin{Bmatrix} \dfrac{\partial}{\partial x} \\ \\ \dfrac{\partial}{\partial y} \end{Bmatrix} \boldsymbol{\Phi}_h^s \tag{26}$$

where $\boldsymbol{\Psi}_h^s$ represents the hierarchic shear strain modes, and $\boldsymbol{\alpha}_h^s$ are associated hierarchic strain parameters.

The objective shear strain field is, on the other hand, defined as:

$$\boldsymbol{\varepsilon}_o^s = \begin{Bmatrix} \gamma_{xzo} \\ \gamma_{yzo} \end{Bmatrix} = \boldsymbol{\Psi}_o^s \boldsymbol{\alpha}_o^s \tag{27}$$

where $\boldsymbol{\Psi}_o^s$ is given in (21), and $\boldsymbol{\alpha}_o^s$ are associated objective strain parameters.

With $\boldsymbol{\Psi}_o^s$ and $\boldsymbol{\Psi}_h^s$ selected, the assumed transverse shear strains can be obtained from the corresponding conforming shear strains in accordance with the hierarchic optimisation approach via (6)-(11). For both corrective (C) and objective (O) approaches, the optimisation procedure can be applied with hierarchic modes up to any complete polynomial order (m = 3, 4, …), where it can be shown that the minimum number of sampling Gauss points required is $(m+1)^2$. This leads to variant 9-noded elements characterised by acronym keys such as H3O9 for an objective strain element with 3rd order hierarchic modes and H4C9 for a corrective strain element with 4th order hierarchic modes, respectively. It is even possible for the optimisation to be undertaken without hierarchic correcting strain modes, in which case the assumed strains are the objective strains that offer a best fit of the conforming strains, leading to an element denoted by H2O9.

3.4 Membrane Locking

From (15a), it is evident that a curved shell element cannot deform in any arbitrary transverse mode (w), as allowed by its translational DOFs, without polluting the membrane strains $(\varepsilon_x, \varepsilon_y, \gamma_{xy})$ with higher-order terms. Although the planar displacement fields (u, v),

via the associated translational DOFs, offer an effective first-order approximation of $(\varepsilon_x, \varepsilon_y, \gamma_{xy})$, the polluting terms from (w) can lead to a significant overestimation of the membrane strain energy. In addressing membrane locking, hierarchic planar translational parameters can be introduced to filter out the higher-order strain terms and achieve the first-order approximation of $(\varepsilon_x, \varepsilon_y, \gamma_{xy})$ afforded by the element, as given by the objective strain modes $\boldsymbol{\Psi}_o^m$.

The hierarchic planar displacements, which are used to establish the hierarchic correcting membrane strains, are defined in terms of natural coordinates (ξ, η). Again, the proposed optimisation approach can utilise hierarchic modes up to any order, where complete cubic and quartic modes are provided below:

$$\begin{Bmatrix} u_h(\xi,\eta) \\ v_h(\xi,\eta) \end{Bmatrix} = \boldsymbol{\Phi}_h^m \boldsymbol{\alpha}_h^m, \quad \boldsymbol{\Phi}_h^m = \left[\begin{array}{cc:cc:c} \boldsymbol{\Phi}_h^3 & \mathbf{0} & \boldsymbol{\Phi}_h^4 & \mathbf{0} & \cdots \\ \mathbf{0} & \boldsymbol{\Phi}_h^3 & \mathbf{0} & \boldsymbol{\Phi}_h^4 & \cdots \end{array}\right] \tag{28}$$

where $\boldsymbol{\Phi}_h^3$ and $\boldsymbol{\Phi}_h^4$ are defined in (23) and (24), respectively.

The corresponding hierarchic membrane strain fields are then obtained from:

$$\boldsymbol{\varepsilon}_h^m = \begin{Bmatrix} \varepsilon_{xh} \\ \varepsilon_{yh} \\ \gamma_{xyh} \end{Bmatrix} = \begin{bmatrix} \frac{\partial}{\partial x} & 0 \\ 0 & \frac{\partial}{\partial y} \\ \frac{\partial}{\partial y} & \frac{\partial}{\partial x} \end{bmatrix} \begin{Bmatrix} u_h \\ v_h \end{Bmatrix} = \boldsymbol{\Psi}_h^m \boldsymbol{\alpha}_h^m, \quad \boldsymbol{\Psi}_h^m = \begin{bmatrix} \frac{\partial}{\partial x} & 0 \\ 0 & \frac{\partial}{\partial y} \\ \frac{\partial}{\partial y} & \frac{\partial}{\partial x} \end{bmatrix} \boldsymbol{\Phi}_h^m \tag{29}$$

where $\boldsymbol{\Psi}_h^m$ represents the hierarchic membrane strain modes, and $\boldsymbol{\alpha}_h^m$ are corresponding strain parameters.

The objective membrane strain fields are given as:

$$\boldsymbol{\varepsilon}_o^m = \begin{Bmatrix} \varepsilon_{xo} \\ \varepsilon_{yo} \\ \gamma_{xyo} \end{Bmatrix} = \boldsymbol{\Psi}_o^m \boldsymbol{\alpha}_o^m \tag{30}$$

where $\boldsymbol{\Psi}_o^m$ is given by (16)-(17), and $\boldsymbol{\alpha}_o^m$ are associated strain parameters.

Similar to optimisation for shear locking, the assumed strains can now be obtained in accordance with Section 2, where similar alternative approaches and levels of hierarchic optimisation may be employed.

3.5 Distortion Locking

As presented in Section 3.2, the objective shear and membrane strain modes are firstly defined as complete polynomial functions in terms of physical (x,y) coordinates, which readily addresses locking due to polluting higher-order terms as a result of distortion in the isoparametric element shape. For a complete treatment of distortion locking, however, it may also be necessary to filter out the polluting bending strains due to element distortion. The bending strains exhibit no sign of locking for regular element shapes, as implied by (15b); however, this is not the case for distorted elements, where the non-constant Jacobian matrix **J** results in conforming bending strains that are non-polynomial in terms of physical coordinates, thus leading to locking due to polluting non-polynomial approximation. Similar to the membrane and shear locking treatment, the polynomial approximation of bending strains afforded by the element in terms of physical coordinates may be restored by employing the optimisation approach. The objective and hierarchic bending strain modes are respectively given by (20) and (31):

$$\boldsymbol{\Psi}_h^b = \boldsymbol{\Psi}_h^m \tag{31}$$

Since $\boldsymbol{\Psi}_o^b$ and $\boldsymbol{\Psi}_h^b$ are identical to $\boldsymbol{\Psi}_o^m$ and $\boldsymbol{\Psi}_h^m$, the transformation of the conforming to assumed bending strains is identical to that relating the conforming and assumed membrane strains, as detailed in the previous section.

3.6 Modification of hierarchic strains

In order to ensure the proposed elements pass the constant mode patch tests, all hierarchic strain modes require zero mean values throughout the element domain [13]. Therefore, an additional measure is taken to enforce zero mean constraints on each strain mode which is achieved via integration over the physical element domain Ω^e as follows:

$$\bar{\boldsymbol{\Psi}}_h^m[i,j] = \boldsymbol{\Psi}_h^m[i,j] - \frac{\int_{\Omega^e} \boldsymbol{\Psi}_h^m[i,j]\,\mathrm{d}\Omega^e}{\Omega^e} \quad (i = 1 \to 3,\ \mathrm{j} = 1 \to 15) \tag{32a}$$

$$\bar{\boldsymbol{\Psi}}_h^b[i,j] = \bar{\boldsymbol{\Psi}}_h^m[i,j] \quad (i = 1 \to 3,\ \mathrm{j} = 1 \to 15) \tag{32b}$$

$$\bar{\boldsymbol{\Psi}}_h^s[i,j] = \boldsymbol{\Psi}_h^s[i,j] - \frac{\int_{\Omega^e} \boldsymbol{\Psi}_h^s[i,j]\,\mathrm{d}\Omega^e}{\Omega^e} \quad (\mathrm{i} = 1 \to 2,\ \mathrm{j} = 1 \to 9) \tag{32c}$$

Accordingly, the modified hierarchic strain modes $\bar{\boldsymbol{\Psi}}_h^m$, $\bar{\boldsymbol{\Psi}}_h^b$, and $\bar{\boldsymbol{\Psi}}_h^s$ replace the original modes $\boldsymbol{\Psi}_h^m$, $\boldsymbol{\Psi}_h^b$, and $\boldsymbol{\Psi}_h^s$ in performing the hierarchic optimisation, thus replacing (6) with:

$$\left(\int_{\Omega^e}\left[\begin{array}{c|c}\bar{\boldsymbol{\Psi}}_h^{\mathrm{T}}\bar{\boldsymbol{\Psi}}_h & -\bar{\boldsymbol{\Psi}}_h^{\mathrm{T}}\boldsymbol{\Psi}_o \\ \hline -\boldsymbol{\Psi}_o^{\mathrm{T}}\bar{\boldsymbol{\Psi}}_h & \boldsymbol{\Psi}_o^{\mathrm{T}}\boldsymbol{\Psi}_o\end{array}\right]\mathrm{d}\Omega^e\right)\left\{\begin{array}{c}\boldsymbol{\alpha}_h \\ \hline \boldsymbol{\alpha}_o\end{array}\right\}=\int_{\Omega^e}\left[\begin{array}{c}-\bar{\boldsymbol{\Psi}}_h^{\mathrm{T}} \\ \hline \boldsymbol{\Psi}_o^{\mathrm{T}}\end{array}\right]\boldsymbol{\varepsilon}\,\mathrm{d}\Omega^e \tag{33}$$

In comparison with other locking-free shell elements, the proposed optimised shell elements have several distinct features. Firstly, the adoption of the co-rotational system for geometrically nonlinear analysis forms the basis of the hierarchic optimisation approach. As presented in Section 4, a co-rotational coordinate system is employed to exclude rigid-body rotations from the local element response, hence enabling simpler or even linear relationships between the strain and local displacement fields in geometrically nonlinear analysis. Within the co-rotational framework, all higher-order strain terms in the local system are therefore regarded as polluting terms, and these are filtered out by enriching conforming strains with hierarchic (corrective) strain modes and targeting the corrected strain fields at an objective smooth distribution. In this respect, computational benefits arise from the fact that the optimal mapping for individual elements need only be established once, at the start of incremental nonlinear analysis. Secondly, the optimised shell elements not only overcome shear locking and membrane locking, as some other methods [5-8,16,19-23] do, but also relieve inaccuracy arising from element distortion, which might be particularly beneficial for analysing practical problems where numerical models with irregular meshes are inevitably required. Different from other methods for curing distortion locking [14,24] where additional parameters and corrected shape functions are defined to describe element distortion and nonlinear equations are required to be solved for deriving the additional parameters, the proposed method automatically deals with element distortion; this is achieved by defining the objective strain modes as polynomial functions in terms of physical element coordinates, where significant computational savings are realised by avoiding the need for additional strain parameters and for solving nonlinear equations. Finally, the proposed optimised shell elements pass the constant strain patch tests and zero energy mode tests, ensuring the reliable and stable performance of these elements in solving various plate and shell problems.

4 BISECTOR CO-ROTATIONAL COORDINATE SYSTEM

The above local formulations of 9-noded optimised shell elements are framed in a bisector co-rotational system, which was originally proposed by the first author for a 4-noded shell element [26] and later applied to a 9-noded conforming curved shell element [27]. In this co-rotational system, the local *x*- and *y*-axes are chosen as the bisectors of the two diagonals of the undeformed element, and rigid body rotations are extracted by orienting these local planar axes so as to also bisect the element diagonals in the current deformed configuration (Figure 3).

The triad $(\mathbf{c}_x, \mathbf{c}_y, \mathbf{c}_z)$ defining the current orientation of the local co-rotational system relative to the global system is simply obtained as:

$$\mathbf{c}_x = \frac{\mathbf{c}_{13} - \mathbf{c}_{24}}{\left|\mathbf{c}_{13} - \mathbf{c}_{24}\right|}, \quad \mathbf{c}_y = \frac{\mathbf{c}_{13} + \mathbf{c}_{24}}{\left|\mathbf{c}_{13} + \mathbf{c}_{24}\right|}, \quad \mathbf{c}_z = \mathbf{c}_x \times \mathbf{c}_y \tag{34}$$

with:

$$\mathbf{c}_{ij} = \frac{\mathbf{v}_{ij}}{\left|\mathbf{v}_{ij}\right|}, \quad \mathbf{v}_{ij} = \mathbf{v}_{ij}^o + \mathbf{d}_j - \mathbf{d}_i \tag{35}$$

where $\mathbf{v}_{ij}^o$ is the vector connecting node *i* to node *j* in the initial element configuration, and $\mathbf{d}_i = \langle U_i, V_i, W_i \rangle^{\mathrm{T}}$ represents the global translational displacements of node *i*. Details of the transformation between global and local systems are provided in [26].

This simple definition automatically satisfies the orthogonality requirement for the two planar axes, and importantly it leads to a relative local orientation of the deformed to the undeformed configuration which is invariant to nodal ordering. The employment of this co-rotational system to the optimised elements leads to identical optimisation directions with different node sequences. Therefore, the variants of the optimised 9-noded element preserve the invariance characteristics.

5 NUMERICAL EXAMPLES

The proposed 9-noded optimised shell elements have been implemented in ADAPTIC [29] v2.14.4, which is used hereafter in several numerical examples to demonstrate the accuracy

of the various element variants. For comparison purposes, 9-noded Reissner-Mindlin shell elements utilising the original and modified MITC9 strain-mapping schemes [22-24] for the local element response, as presented in Appendix A, are also considered with the same co-rotational approach for large displacement analysis. In presenting the results, the various element variants are referred to by acronym keys, as listed in Table 1.

It is worth noting that the elements MITC9* and MITC9is* employ the original 'MITC9' [22] and the modified 'MITC9is' [24] strain-mapping schemes, respectively, where in the local MITC9* formulation a varying basis is used for sampling and mapping covariant strains, whereas for the MITC9is* formulation, a constant Jacobian matrix evaluated at the element centre is used for mapping covariant strains so as to satisfy the patch test [24]. In addition, the asterisk symbol '*' in the acronym keys MITC9* and MITC9is* indicates that there are minor differences of both elements from the original MITC9 and MITC9is elements owing to the employment of a local co-rotational coordinate system along with a low-order strain-displacement relationship, the neglect of the transverse normal strain, and the decoupled mapping of planar strains and transverse shear strains, as detailed in Appendix A.

5.1 Basic element tests

A set of basic element tests has been used to investigate the performance of the proposed optimised elements (H2O9, H3O9, H4O9, H3C9, H4C9) and the MITC9* and MITC9is*, including zero energy mode tests, isotropic element tests and constant strain patch tests.

In the zero energy mode tests, the eigenvalues of the stiffness matrix of an unsupported shell element are calculated for each of the element type, and the number of zero eigenvalues is counted. All the considered element types have exactly 6 zero eigenvalues for both regular and irregular element shapes, hence passing the zero energy mode test. In the isotropic element test, a shell element with irregular element shape is subjected to different loading sets. In each loading case, the variation of the element stiffness matrix to different numbering sequences is investigated. It is found that the element stiffness matrices of all the optimised shell elements are invariant to nodal ordering, owing to the invariance characteristic of the bisector co-rotational system employed for the elements [26], which a priori prescribes the

optimisation directions. The MITC9* and MITC9is* elements also pass the isotropic element test because of the fixed positions of tying points for strain mapping. In the constant strain patch tests, the five-element patch suggested by MacNeal and Harder [30] is adopted to investigate the displacement and strain distributions in the patch using different shell elements. A further distorted five-element patch is also used to study the sensitivity of the element types to element distortion due to shifting of the edge nodes and interior nodes from the mid-positions. Details of the patch tests and associated results are provided in Appendix B. All the optimised 9-noded elements (H2O9, H3O9, H4O9, H3C9 and H4C9) pass the patch tests for both patch patterns owing to the enforcement of zero mean on each hierarchic strain mode. The MITC9is* passes the patch tests for the relatively regular patch pattern, but small errors are generated in the irregular mesh. The MITC9* yields small errors for the relatively regular mesh, but as expected [24] it fails in the constant strain patch test for the highly distorted mesh, evident from the large relative errors in predicting displacements and strains (see Appendix B).

5.2 Clamped square plate under uniform loading

The convergence rates of the optimised elements are investigated in this linear problem, where a $2L\times 2L$ square plate is clamped at all four edges and subjected to a uniformly distributed pressure, as shown in Figure 4. Three thickness-to-length ratios (t/L) are considered to investigate the performance of various element formulations in addressing locking. The geometric and material parameters are given as: $L = 1.0$, $E = 1.7472\times 10^7$, and $\nu = 0.3$. Due to symmetry, a quarter of the plate is modelled with 2×2, 4×4, 8×8, and 16×16 meshes of various 9-noded element types. Soft boundary conditions are used along the clamped edges AB and BC, and symmetric boundary conditions employed for the edges OA and OC as follows: $u = w = \theta_y = 0$ along edge AB, $v = w = \theta_x = 0$ along edge BC, $u = \theta_x = 0$ along edge OA, and $v = \theta_y = 0$ along edge OC. The Jacobian matrix is constant in this example, which leads to identical results between the MITC9* and MITC9is* models. The convergence curves of the considered 9-noded elements are presented in Figure 5, with the relative error in the strain energy as a measure of accuracy:

$$RE = \frac{\left| U_{ref} - U \right|}{U_{ref}} \tag{36}$$

where U represents the total strain energy of a coarse mesh with an element length of h_e; U_{ref} represents the reference value, which is taken as the strain energy obtained from a fine mesh (128×128) of the H3O9 element. The results of the original MITC9 shell element [23] are also plotted in Figure 5, though employing a different accuracy measure:

$$RE = \frac{\left\| \mathbf{u}_{ref}^{\varepsilon} - \mathbf{u}^{\varepsilon} \right\|_{\mathrm{s}}^2}{\left\| \mathbf{u}_{ref}^{\varepsilon} \right\|_{\mathrm{s}}^2} \tag{37}$$

where $\mathbf{u}_{ref}^{\varepsilon}$ is the vector of reference nodal displacement values; $\mathbf{u}^{\varepsilon}$ is the finite element solution of nodal displacements; $\| \cdot \|_{\mathrm{s}}$ is the s-norm [22]. In linear elastic analysis with conforming element formulation, (36) and (37) are equivalent. Even though this equivalence does not strictly hold for hierarchic optimised formulations or mixed formulations, it can still be used for a general comparative assessment of the convergence rate. For both measures of accuracy, the optimal convergence rate is of a fourth order, with the discretisation error being $O(h_e^4)$ (h_e is the nominal element length), which is depicted in Figure 5 with a solid straight line.

All the considered 9-noded elements show roughly optimal convergence rates with no significant upward shifting as the thickness is reduced (except for H3C9 and H4C9). In this problem, the MITC9* and the H2O9 elements seem to have marginally better accuracy, followed by the H3O9 and H4O9 elements. It is also observed that the results of the optimised elements with the objective alternative (H2O9, H3O9, and H4O9) are comparable to the MITC9 results [23] in terms of both the convergence rate and accuracy, while the accuracy of the MITC9* element, as implemented in this work, is even higher than the original MITC9 element, which may result from rounding errors, different accuracy measurement and the formulation differences.

5.3 Cylindrical shell under sinusoidal loading

A cylindrical shell, which has a length of 2*L*, a radius of *R*, and a constant thickness *t*, is subject to a periodic pressure $p(\theta) = \mathrm{p}_0 \cos(2\theta)$. The geometric, material, and loading properties are given as: $L = R = 1.0$, $E = 2.0\times10^5$, $\nu = 1/3$, and $p_0 = 1.0$. Two alternative boundary conditions at both curved ends are considered: a free boundary condition corresponding to a bending-dominant problem, and a fully clamped boundary condition corresponding to a membrane-dominant problem. Due to symmetry, and noting that the response is virtually linear under the applied loading, a sixteenth of the model is analysed with a uniform mesh pattern, as shown in Figure 6.

Figures 7-8 present the convergence rates of various 9-noded optimised elements with free and clamped boundary conditions, respectively. The relative error measure (36) is employed, and the optimal convergence rate is also depicted in the figures. In the bending-dominant problem, all the considered elements show comparable accuracy and good convergence rates, though not optimal. Furthermore, the convergence curves have no evidence of shifting upwards with thickness changes. These elements also perform generally well in the membrane-dominant problem. Figures 9-10, also provide the comparison of the H3O9 and MITC9* results against the MITC9 results [31] with the same accuracy measure. The results show that the H3O9 and MITC9* have comparable convergence rates and accuracy. The MITC9 results have better accuracy in particular for a relatively large thickness-to-length ratio ($t/L = 0.01$), except for the free end case with a small thickness-to-length ratio ($t/L = 0.0001$) where the MITC9 element shows a significant degradation of the convergence rate.

5.4 Plane-stress cantilever

The problem is depicted in Figure 11, where a cantilever beam, with a length *L*, a depth-to-length ratio of 1/10, and a width *t*, is fully clamped at one end and loaded with a transverse force at the other end. This is a plane-stress problem and was presented by Cook et al. [32] to establish the influence of distortion locking on the conforming 9-noded planar element, where meshes (A)–(C) were considered. A further mesh (D) is also considered here, in which the interior element nodes are kept in their original location, leading to increased sensitivity

to distortion locking. Geometric and material parameters are given as: $L = 100$, $t = 1$, $E = 10^7$ and $\nu = 0.3$. An end load $P = 2500$ is uniformly applied on the free edge. The predicted displacements with various meshes and 9-noded element types, normalised by Euler-Bernoulli solution of the transverse tip displacement, are provided in Table 2. It is worth noting that even though the Euler-Bernoulli solution is not accurate owing to the neglect of the contribution from transverse shear, the objective for the normalisation is simply to offer a non-dimensional basis for comparing the various predictions.

It is clear that among the optimised element variants the ones using third or fourth order hierarchic modes provide an effective relief from distortion locking observed with the conforming element, where the objective alternative approach offers marginally better predictions than the corrective approach. The H3O9 element provides virtually identical accuracy to the H4O9 element with fewer Gauss points required. On the other hand, the MITC9* element in mesh (B)–(D) exhibits significant distortion locking owing to highly irregular element shapes. The accuracy of the MITC9is* element is less sensitive to distorted meshes (B) and (C), but is significantly degraded in mesh (D) where the internal node is highly eccentric from the element centre, in which case the Jacobian extracted at the element centre no more represents an average over the element.

5.5 Square plate under transverse point load

The linear bending response of a clamped square plate subject to a central transverse point load P is investigated, where a quarter-model is considered using regular and distorted meshes, as shown in Figure 12. Hard boundary conditions are applied along the clamped edges, and symmetric boundary conditions are applied along edges OA and OC. The geometric and material parameters are given as: $L = 20$, $t = 0.2$, $E = 2.1\times10^6$ and $\nu = 0.3$. The non-dimensional central deflection ($\bar{w}_C$) is given as:

$$\bar{w}_C = \frac{w_C E t^3}{12 P L^2 (1-\nu^2)}$$

The predictions of $\bar{w}_C$ with various 9-noded quadrilateral elements, normalised by the reference value of 0.00560 [33], are presented in Table 3. Clearly, the conforming element

CNF9 exhibits shear locking, which is compounded in the distorted meshes. Again, the proposed optimisation approach shows good accuracy even with the coarse meshes, whether regular or distorted. In this respect, the objective alternative approach, using third or fourth order hierarchic optimisation, is typically better than the corrective alternative, particularly for the coarser meshes. In this example, the coarse meshes of the MITC9* element provide sufficient accuracy despite distorted element shapes. On the other hand, the results of the MITC9is* element are less accurate than the MITC9* elements for mesh (B) and (D), still resulting from the inability of the constant Jacobian $\mathbf{J}_C$ to represent an element average.

5.6 Pinched cylinder with rigid diaphragms

A cylindrical shell, supported by two rigid diaphragms at both ends, is loaded with two unit forces P, as shown in Figure 13. Geometric and material parameters are given as: R = 300, L/R = 2, R/t = 100, E = 3×10^6 and ν = 0.3. Due to symmetry, an octant of the shell is modelled with uniform meshes (2×2, 4×4 and 8×8) of the 9-noded shell elements H3O9, MITC9* and MITC9is*. This problem was also analysed by Kulikov and Plotnikova [34] with uniform meshes of a four-noded degenerated shell element TMS4SA, and by Kim et al. [35] with meshes of an 8-noded solid-shell element XSOLID85. Table 4 shows the meshes of various shell or solid-shell elements that correspond to the same number of overall DOFs. By normalising the predicted deflection at the point of loading by the analytical solution 0.18248×10^{-4} [36], the results of various models with various element types are listed in Table 5. By comparing the results of the H3O9 element to those of other models having the same number of DOFs, it is evident that the H3O9 element yields sufficient accuracy even in coarse meshes.

5.7 Hemispherical shell under two pairs of pinching forces

A hemispherical shell, with radius R and thickness t, is subjected to two inward and two outward forces 90° apart, as depicted in Figure 14. Due to symmetry, only a quarter of the hemisphere is modelled with $3\times N\times N$ meshes of the considered 9-noded quadrilateral shell elements, where 3 denotes three subdomains in the quarter model, and N the number of

elements per side for each subdomain. A 3×6×6 discretisation pattern is illustrated in Figure 15, where 6×6 9-noded shell elements are employed in each of the three subdomains.

Linear elastic problem

The performance of the considered shell formulations is firstly investigated considering a linear elastic material and excluding geometric nonlinearity. The material and geometric parameters are given as follows: $E = 6.825\times10^7$, $\nu = 0.3$, $R = 10$ and $t = 0.04$. The magnitudes of the concentrated forces F in Figure 14 are fixed to a unit value. It is worth noting that the shell elements are doubly curved, which may lead to significant locking if the shell thickness is small, particularly for coarse meshes. Various meshes (3×2×2, 3×3×3, 3×4×4 and 3×6×6) of the proposed optimised shell elements and the MITC9* and MITC9is* are employed to investigate their efficiency and accuracy. A linear numerical solution of the radial displacement at the point of load was previously obtained as 0.0924 [37], which is used here as a reference value. Table 6 reports the predicted radial displacements by various meshes and element types, normalised by the reference value.

Among the optimised element variants, the objective alternative approach (except H2O9) provides more accurate predictions than the corrective approach in particular for coarser meshes. As the mesh is refined, the results obtained from the corrective approach become closer to those of the objective counterpart. Evidently, the H3O9 and H4O9 exhibit much higher accuracy than all other element types for all the meshes, indicating an effective relief of locking, with the H3O9 element being more efficient because of less Gauss points required. The MITC9* and MITC9is* results become accurate for a 3×4×4 mesh, though noticeable locking is exhibited for coarser meshes.

Materially and geometrically nonlinear problem

The performance of the 9-noded shell elements in modelling both geometric and material nonlinearity is considered here. The radius of the hemisphere is $R = 10$, and a bi-linear elasto-plastic material model with isotropic strain hardening is applied, with the material parameters given as: $E = 1.0\times10^1$, $\nu = 0.2$, $\sigma_y = 0.2$, and $H = 9.0$, where H is a hardening parameter related to plastic strains. Two cases are considered for the shell thickness: $t = 0.05$ and 0.5.

Five Gauss points are employed across the shell thickness, which provides a convergent though-thickness solution for both the optimised and the mixed shell elements.

For the case of t = 0.5, nonlinear analysis was carried out with thirty load steps, and the load-deflection curves at the pinching points A and B for various meshes (3×3×3, 3×6×6 and 3×12×12) of the H3O9 and MITC9* are plotted in Figure 16, where it is evident that a 3×6×6 mesh can provide a convergent solution for both the H3O9 and the MITC9*. It is worth noting that in this case the MITC9is* results are almost identical to MITC9*, which are therefore not presented. In Figure 17, the load-deflection curves for the 3×6×6 mesh of both the H3O9 and the MITC9* are compared against the results of others, including those from Bestch and Stein [37] using a 3×16×16 mesh of a 4-noded quadrilateral element, Eberlein and Wriggers [38] using a 3×12×12 mesh of a 4-noded quadrilateral element with 5 Gauss points along the shell thickness, and Li et al. [39] using a 3×6×6 mesh of a 6-noded triangular shell element with 6 Gauss points along the shell thickness. In addition, the results using the 3×12×12 mesh of the H3O9 element are used as a reference solution, which are also shown in Figure 17. Evidently, the results from the 3×6×6 H3O9 and MITC9is* models exhibit comparable accuracy with the results by Bestch and Stein [37], but with a reduced number of overall DOFs. In addition, the FE models by Eberlein and Wriggers [38] and Li et al. [39], which have the same overall DOFs with the H3O9 and MITC9is* models, show degraded accuracy, evident from the stiffer response. Figure 18 shows the deformed configuration of the pinched hemisphere for a 3×6×6 mesh of the H3O9 with $F = 30\times10^{-3}$. It is worth noting that in this geometrically and materially nonlinear problem, the planar and transverse shear strains are generally less than 10% throughout the analysis, except for the horizontal planar strain in the shell element to which the outward load is directly applied (i.e. the shell element that Point A is attached to) in the last load step ($F = 30\times10^{-3}$). Generally, this problem can be regarded as a small-to-moderate strain problem, and the co-rotational approach is therefore considered to be applicable.

For the thinner shell case (t = 0.05), a convergence study is also carried out, with the load-deflection curves for various meshes (3×3×3, 3×6×6 and 3×12×12) of the H3O9, MITC9* and MITC9is* being displayed in Figure 19. It is observed that the coarse 3×3×3 mesh of the

H3O9 already captures the response of the structure throughout the deformation history. Even though the load-deflection curves predicted by the 3×3×3 mesh of the MITC9* are also quite close to the reference solution, there is a noticeable difference in the slopes of the curves in the small displacement range. The results of the 3×3×3 mesh of the MITC9is* deviate significantly from the other curves, even in the linear elastic range, hence indicating the lack of accuracy owing to the use of an averaged Jacobian in the strain mapping. For the finer 3×6×6 mesh, where the element shape is more regular and the local plasticity is much better to be captured, the MITC9* and MITC9is* results show sufficiently high accuracy comparable to that of the H3O9 element. Table 7 lists the CPU times for the H3O9 and MITC9is* models with various mesh sizes, where the reported CPU times are normalised relative to that of the 3×3×3 MITC9is* model. As evident from Table 7, for the same mesh, the MITC9is* model is more computationally efficient than the H3O9 model, principally owing to fewer sampling Gauss points employed for each shell element, as indicated in Table 1. It is also observed that as the mesh is refined the H3O9-to-MITC9is* computation time ratio reduces from 2.1 to 1.3, in which case solving the large set of nonlinear equilibrium equations controls the computation time while the processing time for the locking elimination scheme becomes less dominant.

5.8 Annular plate subject to end loading

An annular plate is fully clamped at one end and subjected to a uniform transverse loading p at the other end, as is shown in Figures 20-21. The geometric and material properties are specified as: $R_1 = 6$, $R_2 = 10$, $t = 0.03$, $E = 2.1\times10^7$ and $v = 0.0$. The plate is modelled with 15×3 and 60×6 meshes of various optimised 9-noded elements, and nonlinear analysis is performed with 30 load steps up to a uniform loading of $p = 6$.

The load-displacement curves at points A and B for the 15×3 mesh of various optimised elements are plotted in Figure 22, with the results from a fine mesh (60×9) of H3O9 used as a reference solution. The accuracy and efficiency of the optimised shell elements are compared in Table 8, where predictions of the final displacement along the z-axis at Point A and the overall CPU times are provided. It is worth noting that the displacement at Point A for each

model has been normalised by the reference value predicted by the 60×6 H3O9 model. In addition, for each mesh size, the reported CPU times are normalised relative to that of the associated H2O9 model. As indicated in Table 1, as the hierarchic order increases, more sampling Gauss points are employed, which accounts for the increased CPU time for the optimised elements with third or fourth hierarchic orders, in comparison with that for the H2O9 counterpart. However, as the mesh is refined, the difference in the computational efficiency for various hierarchic orders reduces, owing to the dominance on computing demand of solving equilibrium equations rather than the locking elimination process. In addition, it is observed from Table 8 and Figure 22 that the H3O9 and H4O9 results are more accurate than other optimised elements for the coarser mesh. For the finer 60×6 mesh, all the optimised element models converge to the reference solution.

The H3O9 results are also compared with the MITC9* and MITC9is* results in Figure 23. Also presented are results with a 15×3 mesh of 9-noded hybrid stress elements by Sansour and Kollmann [40] and a 30×6×1 mesh of 8-noded solid-shell elements by Norachan et al. [41], where all models have comparable number of DOFs. In this example, the meshes of the H3O9 and the MITC9* elements yield more accurate results than others.

5.9 Pinched hemispherical shell with 18° cut-off

Consideration is given here to a large displacement problem where a hemispherical shell with an 18°circular cut-off at its top is subjected to symmetric concentrated forces at its base, as shown in Figures 24-25. The geometric and material parameters are: R = 10, t = 0.04, $E = 6.825\times10^7$, and ν = 0.3. Due to symmetry, a quarter of the shell is modelled with three uniform meshes (4×4, 8×8 and 16×16) of various 9-noded element types. This problem has been studied by Celigoj [42] using a 16×16 mesh of a 9-noded shell element, which is used hereafter as a reference solution.

The load-displacement curves of the radial displacement at point B predicted by the 4×4 mesh of the conforming and the optimised element variants are depicted in Figure 26, compared against the reference solution by Celigoj. Clearly, noticeable locking phenomenon is exhibited in the conforming element model, mainly attributed to membrane locking. The

optimised elements H3O9 and H4O9 provide better approximations of the shell response than the corrective alternative approach for this coarse mesh (4×4), though this difference will diminish with mesh refinement. It is also observed that the equilibrium paths of the coarse mesh with H2O9 deviate from the other curves in terms of the curve shapes, indicating the importance of the inclusion of correction hierarchic strain modes in the optimisation.

In Figure 27, load-displacement curves of the radial displacement at points A and B predicted by the meshes of H3O9, MITC9* and MITC9is* are compared with Celigoj's solution. For the coarse mesh (4×4), the optimised elements H3O9 and H4O9 show better accuracy than the mixed elements MITC9* and MITC9is*. As the mesh is refined to (8×8), all the elements converge to Celigoj's solution.

The sensitivity of the element performance to distortion is also investigated with 4×4 and 8×8 irregular meshes, which are obtained by moving the three nodes (C, D, E) in a regular mesh to positions (C', D', E'). An 8×8 mesh is illustrated in Figure 28, while the larger points in the figure also indicate the node positions for a 4×4 mesh. By changing the positions of the inward and outward forces, two sets of results are readily obtained with the distorted meshes. Figures 29-30 depict the two sets of load-displacement curves with the H3O9, MITC9* and MITC9is* elements. It is evident that in the coarser mesh, the H3O9 element provides better predictions than the mixed elements for both distortion cases. On the other hand, the MITC9is* element performs better than MITC9* element in one distortion case but is not as accurate in the other one. Nevertheless, all the solutions converge in the finer mesh.

6 CONCLUSIONS

This paper presents a hierarchic optimisation approach which can be applied to conforming elements with the aim of relieving the inaccuracies arising from locking phenomena. The proposed approach is based on filtering out polluting strains at the element level using hierarchic strain modes, hence restoring the strain field to the distribution afforded by the conforming formulation.

The application of the proposed approach is demonstrated using a 9-noded Lagrangian shell element, where a co-rotational framework is employed to maintain a simpler strain-

displacement relationship in the local element system even for geometrically nonlinear analysis, and the membrane, bending, and transverse shear strains are separately enhanced in the local system. On one hand, hierarchic strain modes in terms of natural coordinates are added to the conforming strains so as to filter out higher-order polluting strain terms and to smooth the strain distribution in the element domain; on the other hand, objective (or target) strain modes are defined in terms of physical coordinates, hence effectively reducing sensitivity to element shape distortion. Accordingly, by minimising the difference between the corrected strains and the objective strains, all strain parameters can be determined, and strain fields are smoothed to approach the optimal distribution. It is worth noting that the proposed optimised shell elements not only remedy shear locking and membrane locking, as other locking-elimination methods may achieve, but also relieve distortion locking arising from irregular element shapes, which may be required for modelling complex geometric structural configurations.

Several numerical examples are used to demonstrate the effectiveness of the proposed 9-noded optimised elements. For comparison purposes, the results by two Reissner-Mindlin shell elements based on the MITC9 strain-mapping schemes, are also presented. Numerical tests have shown that all of the optimised 9-noded elements pass the fundamental element tests, confirming the stability, element isotropy, and absence of rank deficiency in the proposed approach. Among the optimised elements, the H2O9 element, which employs no hierarchic strain enhancement towards the objective strains, results in degraded performance in curved shell problems compared to element variants with hierarchic corrections, which highlights the importance of the inclusion of higher-order strain modes in the optimisation. Furthermore, for the same hierarchic order *m*, the objective H*m*O9 element yields superior results to the corrective H*m*C9 element in terms of both accuracy and convergence rate, with the objective H3O9 element based on third-order hierarchic optimisation providing both effectiveness and efficiency. The performance of H3O9 is also generally comparable to the mixed elements based on the MITC9 formulations, but importantly it shows better accuracy in coarse meshes with irregular element shapes, demonstrating an effective relief of not only shear and membrane locking but also distortion locking.

REFERENCES

[1] Zienkiewicz OC. *The Finite Element Method*, Vol.1. The Basis. Oxford: Butterworth Heinemann, 2000.

[2] Zienkiewicz OC, Taylor RL, Too JM. Reduced integration technique in general analysis of plates and shells. *International Journal for Numerical Methods in Engineering* 1971; **3**(2):275-290.

[3] Pugh EDL, Hinton E, Zienkiewicz OC. A study of quadrilateral plate bending elements with 'reduced' integration. *International Journal for Numerical Methods in Engineering* 1978; **12**(7):1059-1079.

[4] Stolarski H, Belytschko T. Membrane locking and reduced integration for curved elements. *Journal of Applied Mechanics* 1982; **49**(1):172-176.

[5] Doherty WP, Wilson EL, Taylor RL. Stress analysis of axisymmetric solids utilizing higher-order quadrilateral finite elements. University of California, Structural Engineering Laboratory, 1969.

[6] Hughes TJ, Cohen M, Haroun M. Reduced and selective integration techniques in the finite element analysis of plates. *Nuclear Engineering and Design* 1978; **46**(1):203-222.

[7] Malkus DS, Hughes TJ. Mixed finite element methods—reduced and selective integration techniques: a unification of concepts. *Computer Methods in Applied Mechanics and Engineering* 1978; **15**(1):63-81.

[8] Liu WK, Hu YK, Belytschko T. Multiple quadrature underintegrated finite elements. *International Journal for Numerical Methods in Engineering* 1994; **37**(19):3263-3289.

[9] Tessler A, Hughes TJ. An improved treatment of transverse shear in the Mindlin-type four-node quadrilateral element. *Computer Methods in Applied Mechanics and Engineering* 1983; **39**(3):311-335.

[10] Tessler A, Hughes TJ. A three-node Mindlin plate element with improved transverse shear. *Computer Methods in Applied Mechanics and Engineering* 1985; **50**(1):71-101.

[11] Izzuddin BA, Lloyd Smith D. Reissner-mindlin plate bending elements with shear freedoms. *B.H.V. Topping, (Editor), Proceedings of the Ninth International Conference on Civil and Structural Engineering Computing*, Civil-Comp Press, Stirlingshire, UK, Paper 37, 2003. doi:10.4203/ccp.77.37.

[12] Simo JC, Rifai MS. A class of mixed assumed strain methods and the method of incompatible modes. *International Journal for Numerical Methods in Engineering* 1990; **29**(8):1595-1638.

[13] Simo JC, Armero F, Taylor RL. Improved versions of assumed enhanced strain tri-linear elements for 3D finite deformation problems. *Computer Methods in Applied Mechanics and Engineering* 1993; **110**(3):359-386.

[14] Korelc J, Wriggers P. Improved enhanced strain four-node element with Taylor expansion of the shape functions. *International Journal for Numerical Methods in Engineering* 1997; **40**(3):407-421.

[15] Huang, HC, Hinton E. A nine node Lagrangian Mindlin plate element with enhanced shear interpolation. *Engineering Computations* 1984; **1**(4): 369-379.

[16] MacNeal RH. Derivation of element stiffness matrices by assumed strain distributions. *Nuclear Engineering and Design* 1982; **70**(1):3-12.

[17] Jang J, Pinsky PM. An assumed covariant strain based 9-node shell element. *International Journal for Numerical Methods in Engineering* 1987; **24**(12):2389-2411.

[18] MacNeal RH. A simple quadrilateral shell element. *Computers & Structures* 1978; **8**(2):175-183.

[19] Panasz P, Wisniewski K. Nine-node shell elements with 6 dofs/node based on two-level approximations. Part I: Theory and linear tests. *Finite elements in Analysis and Design* 2008; **44**(12):784-796.

[20] Bathe KJ, Dvorkin EN. A formulation of general shell elements—the use of mixed interpolation of tensorial components. *International Journal for Numerical Methods in Engineering* 1986; **22**(3):697-722.

[21] Bucalem ML, Bathe KJ. Higher-order MITC general shell elements. *International Journal for Numerical Methods in Engineering* 1993; **36**(21):3729-3754.

[22] Bathe KJ, Lee PS, Hiller JF. Towards improving the MITC9 shell element. *Computers & Structures* 2003; **81**(8):477-489.

[23] Lee PS, Bathe KJ. The quadratic MITC plate and MITC shell elements in plate bending. *Advances in Engineering Software* 2010; **41**(5):712-728.

[24] Wisniewski K, Panasz P. Two improvements in formulation of nine-node element MITC9. *International Journal for Numerical Methods in Engineering* 2013; **93**(6):612-634.

[25] Izzuddin BA. An optimisation approach towards lock-free finite elements. *B.H.V. Topping, (Editor), Proceedings of the Eleventh International Conference on Civil, Structural and Environmental Engineering Computing*, Civil-Comp Press, Stirlingshire, UK, Paper 105, 2007. doi:10.4203/ccp.86.105.

[26] Izzuddin BA. An enhanced co-rotational approach for large displacement analysis of plates. *International Journal for Numerical Methods in Engineering* 2005; **64**(10):1350-1374.

[27] Izzuddin BA, Li ZX. A co-rotational formulation for large displacement analysis of curved shells. *Proceedings of the 18th Australasian Conference on the Mechanics of Structures and Materials*, Perth, Australia, 1-3 December, 2004, Developments in Mechanics of Structures and Materials - Deeks & Hao (eds), Vol. 2, Taylor & Francis Group, London, pp. 1247-1253.

[28] Liang Y, Izzuddin BA. An optimisation approach towards locking-free isotropic shell elements. *A. Zingoni, (Editor), Insights and Innovations in Structural Engineering, Mechanics and Computation: Proceedings of the Sixth International Conference on Structural Engineering, Mechanics and Computation*, Cape Town, South Africa, 5-7 September 2016, CRC Press.

[29] Izzuddin BA. Nonlinear dynamic analysis of framed structures. *PhD Thesis*, Department of Civil Engineering, Imperial College, University of London, 1991.

[30] MacNeal RH, Harder RL. A proposed standard set of problems to test finite element accuracy. *Finite Elements in Analysis and Design* 1985; **1**(1):3-20.

[31] Bathe KJ, Iosilevich A, Chapelle D. An evaluation of the MITC shell elements. *Computers & Structures* 2000; **75**(1): 1-30.

[32] Cook RD. *Concepts and applications of finite element analysis*. New York ; Chichester: Wiley; 1989.

[33] Timoshenko S. *Theory of plates and shells*. New York: McGraw-Hill; 1940.

[34] Kulikov GM, Plotnikova SV. Geometrically exact assumed stress–strain multilayered solid-shell elements based on the 3D analytical integration. *Computers & structures* 2006; **84**(19): 1275-1287.

[35] Kim KD, Liu GZ, Han SC. A resultant 8-node solid-shell element for geometrically nonlinear analysis. *Computational Mechanics* 2005; **35**(5): 315-331.

[36] Heppler GR, & Hansen JS. A Mindlin element for thick and deep shells. *Computer methods in applied mechanics and engineering* 1986; **54**(1): 21-47.

[37] Betsch P, Stein E. Numerical implementation of multiplicative elasto-plasticity into assumed strain elements with application to shells at large strains. *Computer Methods in Applied Mechanics and Engineering* 1999; **179**(3): 215-245.

[38] Eberlein R, Wriggers P. Finite element concepts for finite elastoplastic strains and isotropic stress response in shells: theoretical and computational analysis. *Computer Methods in Applied Mechanics and Engineering* 1999; **171**(3):243–279.

[39] Li ZX, Xiang Y, Izzuddin BA, Vu-Quoc L, Zhuo X, Zhang C. A 6-node co-rotational triangular elasto-plastic shell element. Computational Mechanics 2015; **55**(5): 837-859.

[40] Sansour C, Kollmann FG. Families of 4-node and 9-node finite elements for a finite deformation shell theory. An assesment of hybrid stress, hybrid strain and enhanced strain elements. *Computational Mechanics* 2000; **24**(6): 435-447.

[41] Norachan P, Suthasupradit S, Kim KD. A co-rotational 8-node degenerated thin-walled element with assumed natural strain and enhanced assumed strain. *Finite Elements in Analysis and Design* 2012; **50**: 70-85.

[42] Celigoj C. A strain- and displacement-based variational method applied to geometrically nonlinear shells. *International Journal for Numerical Methods in Engineering* 1996; **39**(13):2231-2248.

[43] Li ZX, Izzuddin BA, Vu-Quoc L. A 9-node co-rotational quadrilateral shell element. *Computational Mechanics* 2008; **42**(6):873-884.

[44] Izzuddin BA, Liang Y. Bisector and zero-macrospin co-rotational systems for shell elements. *International Journal for Numerical Methods in Engineering* 2016; **105**(4): 286-320.

[45] Liang Y, Izzuddin BA. Large displacement analysis of sandwich plates and shells with symmetric/asymmetric lamination. *Computers & Structures* 2016; **166**:11-32.

[46] Liang Y, Izzuddin BA. Nonlinear analysis of laminated shells with alternating stiff/soft lay-up. *Composite Structures* 2015; **133**:1220-1236.

[47] Liang Y, Lancaster F, Izzuddin BA. Effective modelling of structural glass with laminated shell elements. *Composite Structures* 2016; **156**: 47-62.

APPENDIX A: MIXED FORMULATIONS OF REISSNER-MINDLIN SHELL ELEMENTS BASED ON MITC9 ELEMENT

The general MITC formulation procedure can be summarised as follows:

(i) Evaluate Green strains directly from displacement fields at a set of prescribed tying points.

(ii) Transform the extracted Green strains into corresponding covariant strain components:

$$\boldsymbol{\varepsilon}_2 = \mathbf{J}^{\mathrm{T}}\,\mathbf{E}_2\mathbf{J} \tag{A.1}$$

where $\mathbf{E}_2$ is the Green strain tensor in terms of Cartesian coordinates; $\boldsymbol{\varepsilon}_2$ is the covariant strain tensor; and $\mathbf{J}$ is the Jacobian matrix, which is expressed as:

$$\mathbf{J} = \begin{bmatrix} \dfrac{\partial x}{\partial \xi} & \dfrac{\partial x}{\partial \eta} & \dfrac{\partial x}{\partial \zeta} \\ \dfrac{\partial y}{\partial \xi} & \dfrac{\partial y}{\partial \eta} & \dfrac{\partial y}{\partial \zeta} \\ \dfrac{\partial z}{\partial \xi} & \dfrac{\partial z}{\partial \eta} & \dfrac{\partial z}{\partial \zeta} \end{bmatrix} \tag{A.2}$$

(iii) Interpolate covariant strain fields with the use of the extracted covariant strains:

$$\varepsilon_{rs}^{AS}(\xi,\eta,\zeta) = \mathbf{H}_{rs}\boldsymbol{\varepsilon}_{rs,T}^{DI} \tag{A.3}$$

where: $r, s = (\xi, \eta, \zeta)$; the superscript '*AS*' and '*DI*' refers respectively to the assumed strain distribution and the distribution obtained directly from displacement fields; $\mathbf{H}_{rs}$ is a row vector of interpolation functions associated with the tying points; $\boldsymbol{\varepsilon}_{rs,T}^{DI}$ consists of the covariant strain values extracted at the tying points.

(iv) Transform the assumed covariant strain fields to the corresponding Green strain fields in terms of real coordinates, obtained from:

$$\mathbf{E}_2^{AS} = \mathbf{J}^{-\mathrm{T}}\boldsymbol{\varepsilon}_2^{AS}\mathbf{J}^{-1} \tag{A.4}$$

(v) Replace displacement-based strains with the assumed strain distributions obtained from (iv) in the element formulation.

The MITC9 [22] quadrilateral shell element performs well, but it does not pass the patch test for irregular element shapes due to the varying basis used for sampling and mapping

covariant strains. Wisniewski and Panasz resolved the issue by using a constant Jacobian matrix evaluated at the element centre [24]. This is equivalent to replacing (A.1) and (A.4) with:

$$\boldsymbol{\varepsilon}_2 = \mathbf{J}_C^{\mathrm{T}} \mathbf{E}_2 \mathbf{J}_C \tag{A.5}$$

$$\mathbf{E}_2^{AS} = \mathbf{J}_C^{-\mathrm{T}} \boldsymbol{\varepsilon}_2^{AS} \mathbf{J}_C^{-1} \tag{A.6}$$

where $\mathbf{J}_C$ is the Jacobian matrix evaluated at the element centre ($\xi = 0, \eta = 0$).

The original MITC9 [22] and the improved MITC9is [24] strain mapping approaches have been adopted in the local kinematics of curved Reissner-Mindlin shell elements [43,44] employing a low-order strain-displacement relationship, the incorporation of which in the co-rotational system hence allowing large displacement analysis.

The mixed Reissner-Mindlin shell elements, denoted as 'MITC9*' and 'MITC9is*', respectively, are associated with several assumptions that differ them from the elements MITC9 [22] and MITC9is [24]: (i) the elements are applicable to small-strain problems only; (ii) the elements are shallow and thin, so that the natural coordinate axis ζ is taken to have an identical orientation to the local *z*-axis; and (iii) the transverse normal strain ε_z is ignored. Accordingly, the Jacobian matrix can be simplified to:

$$\mathbf{J} = \begin{bmatrix} \dfrac{\partial x}{\partial \xi} & \dfrac{\partial x}{\partial \eta} & 0 \\ \dfrac{\partial y}{\partial \xi} & \dfrac{\partial y}{\partial \eta} & 0 \\ 0 & 0 & \dfrac{t}{2} \end{bmatrix} \tag{A.7}$$

where *t* is the shell thickness. This simplification enables decoupled relationships between real strains and covariant strains, with each set of the generalised real strains related to their covariant counterparts only, which are expressed thus as:

$$\begin{bmatrix} \varepsilon_{\xi\xi} & \varepsilon_{\xi\eta} \\ \varepsilon_{\xi\eta} & \varepsilon_{\eta\eta} \end{bmatrix} = \mathbf{J}_p^{\mathrm{T}} \begin{bmatrix} \varepsilon_x & \dfrac{1}{2}\gamma_{xy} \\ \dfrac{1}{2}\gamma_{xy} & \varepsilon_y \end{bmatrix} \mathbf{J}_p \tag{A.8}$$

$$\begin{bmatrix} \kappa_{\xi\xi} & \kappa_{\xi\eta} \\ \kappa_{\xi\eta} & \kappa_{\eta\eta} \end{bmatrix} = \mathbf{J}_p^{\mathrm{T}} \begin{bmatrix} \kappa_x & \frac{1}{2}\kappa_{xy} \\ \frac{1}{2}\kappa_{xy} & \kappa_y \end{bmatrix} \mathbf{J}_p \tag{A.9}$$

$$\begin{Bmatrix} \varepsilon_{\xi\zeta} \\ \varepsilon_{\eta\zeta} \end{Bmatrix} = \frac{t}{2} \mathbf{J}_p^{\mathrm{T}} \begin{Bmatrix} \frac{1}{2}\gamma_{xz} \\ \frac{1}{2}\gamma_{yz} \end{Bmatrix} \tag{A.10}$$

where $\mathbf{J}_p$ is a sub-matrix of $\mathbf{J}$:

$$\mathbf{J}_p = \begin{bmatrix} \frac{\partial x}{\partial \xi} & \frac{\partial x}{\partial \eta} \\ \frac{\partial y}{\partial \xi} & \frac{\partial y}{\partial \eta} \end{bmatrix} \tag{A.11}$$

The local MITC9* formulation is derived by employing the strain transformations (A.8)-(A.10) with $\mathbf{J}_p$ evaluated at each sampling station, whereas the local MITC9is* formulation is obtained by using (A.8)-(A.10) with a constant $\mathbf{J}_p$ evaluated at the element centre only [44]. The positions of the tying points for both elements are shown in Figure A.1, where the associated interpolation functions for the covariant strains can be found elsewhere [22].

For geometrically nonlinear problems that do not involve severe element distortion, the local MITC9* and MITC9is* formulations, in combination with the co-rotational framework, have been shown recently to provide good accuracy in the nonlinear analysis of both monolithic and laminated plate and shell structures [44-47].

APPENDIX B: FIVE-ELEMENT PATCH TESTS

The five-element patch suggested by MacNeal and Harder [30], as shown in Figure B.1, is employed to illustrate the membrane and out-of-plane bending behaviour of the considered 9-noded shell elements. In the patch, edge nodes and internal nodes are placed at the middle positions. The geometric properties of the rectangular plate are: L = 0.24, W = 0.12 and t = 0.001. It has a Young's modulus of $E = 10^6$ and a Poisson's ratio of v = 0.25. In the membrane patch test, the boundary conditions at the external nodes are:

$$u = 10^{-3}\left(x + \frac{1}{2}y\right), \quad v = 10^{-3}\left(y + \frac{1}{2}x\right), \quad w = \theta_x = \theta_y = 0$$

which correspond to a constant membrane strain state where $\varepsilon_x = \varepsilon_y = \gamma_{xy} = 0.001$.

In the out-of-plane bending patch test, the boundary conditions at the external nodes are:

$$u = v = 0, \quad w = 10^{-3}\frac{\left(x^2 + xy + y^2\right)}{2}, \quad \theta_x = 10^{-3}\left(x + \frac{1}{2}y\right), \quad \theta_y = 10^{-3}\left(y + \frac{1}{2}x\right)$$

which correspond to a constant bending strain state where $\kappa_x = \kappa_y = \kappa_{xy} = 0.001$.

The patch tests are conducted on various quadrilateral element types, with the nodal displacements inside the patch and the strains evaluated at each element centre compared against reference values. The maximum relative errors in the nodal displacements and strain components are listed in Tables B.1 and B.2 for the membrane and bending patch tests, respectively. Clearly, all the optimised 9-noded elements and the MITC9is* pass the patch tests. The results with MITC9*, however, yield small errors, as confirmed previously by Wisniewski and Panasz [24].

A further step is taken to investigate the behaviour of the considered 9-noded elements in a more irregular mesh, where the original patch is distorted by shifting four edge nodes 13, 14, 15 and 16, either parallel or perpendicular to the edges, and moving the internal node 25 along the x direction, as illustrated in Figure B.2. All the shifts of nodal positions are of a magnitude d = 0.01. Results of the membrane patch test with this distorted mesh are given in Table B.3. As expected, all the optimised 9-noded elements pass the test owing to the enforcement of zero mean on each hierarchic strain mode. The results with MITC9is* are also good, though small errors are generated in this case. However, MITC9* fails in the

constant strain patch test, evident from the large relative errors in predicting displacements and strains.

Table 1: Considered variants of 9-noded Reissner-Mindlin shell element.

Acronym key	Strain field	Hierarchic order	Sampling Gauss points
CNF9	Conforming	-	3×3
H2O9	Assumed, objective	-	3×3
H3O9	Assumed, objective	3	4×4
H4O9	Assumed, objective	4	5×5
H3C9	Assumed, corrective	3	4×4
H4C9	Assumed, corrective	4	5×5
MITC9*	Assumed, MITC9*	-	3×3
MITC9is*	Assumed, MITC9is*	-	3×3

Table 2: Normalised cantilever displacement predictions using various 9-noded elements.

Acronym key	Mesh (A)	Mesh (B)	Mesh (C)	Mesh (D)
CNF9	0.954	0.791	0.737	0.476
H2O9	0.954	0.812	0.904	0.464
H3O9	0.954	0.830	0.971	0.972
H4O9	0.954	0.827	0.972	0.972
H3C9	0.954	0.824	0.913	0.954
H4C9	0.954	0.827	0.972	0.972
MITC9*	0.990	0.255	0.712	0.535
MITC9is*	0.990	0.805	0.958	0.604

Table 3: Normalised plate central deflection $\bar{w}_C$ using various 9-noded elements.

Acronym key	Mesh (A)	Mesh (B)	Mesh (C)	Mesh (D)
CNF9	0.718	0.269	0.925	0.638
H2O9	1.006	0.955	1.006	0.959
H3O9	0.974	0.965	1.001	0.996
H4O9	0.973	0.958	1.001	0.996
H3C9	0.916	0.856	0.997	0.981
H4C9	0.917	0.899	0.997	0.990
MITC9*	1.005	1.000	1.005	1.003
MITC9is*	1.005	0.882	1.005	0.960

Table 4: Meshes of various elements that have the same overall number of DOFs.

Mesh code	9-noded shell elements (H3O9, MITC9*, MITC9is*)	4-noded shell element (TMS4SA [34])	8-noded solid-shell element (XSOLID85 [35])
Mesh 1	2×2	4×4	4×4×1
Mesh 2	4×4	8×8	8×8×1
Mesh 3	8×8	16×16	8×8×1

Note that the '1' in meshes of XSOLID85 means that a single layer of the XSOLID85 element is applied along the shell thickness direction.

Table 5: Normalised deflections at the point of loading for the pinched cylinder problem.

Acronym key	Mesh 1	Mesh 2	Mesh 3
H3O9	0.816	0.938	0.988
MITC9*	0.711	0.962	1.000
MITC9is*	0.711	0.962	1.000
TMS4SA [34]	0.890	0.941	0.986
XSOLID85 [35]	0.382	0.751	0.932

Table 6: Normalised deflection at the point of loading for the pinched hemispherical shell.

Element type	Mesh			
	3×2×2	3×3×3	3×4×4	3×6×6
H2O9	0.527	0.481	0.917	0.981
H3O9	0.976	0.998	1.001	1.001
H4O9	0.980	0.995	0.999	1.001
H3C9	0.859	0.722	0.990	0.997
H4C9	0.886	0.923	0.990	0.997
MITC9*	0.932	0.879	0.997	0.999
MITC9is*	0.936	0.740	0.998	0.999

Table 7: Normalised CPU time for various models.

Element type	Mesh	Normalised CPU time
MITC9is*	3×3×3	1.0
	3×6×6	6.2
	3×12×12	56.8
H3O9	3×3×3	2.1
	3×6×6	10.3
	3×12×12	73.4

Table 8: Comparison of accuracy and computation time for various models.

Element type	15×3 mesh		60×6 mesh	
	$\bar{w}_A$	Normalised CPU time	$\bar{w}_A$	Normalised CPU time
H2O9	0.94	1.0	1.00	1.0
H3O9	1.00	2.3	1.00	1.7
H4O9	0.99	4.3	1.00	3.0
H3C9	0.96	2.2	1.00	2.0
H4C9	0.99	4.4	1.00	3.0

Table B.1: Relative error of displacements and strains in membrane patch test.

Acronym key	Maximum error in u	Maximum error in v	Maximum error in ε_x	Maximum error in ε_y	Maximum error in γ_{xy}
H2O9	0.000	0.000	0.000	0.000	0.000
H3O9	0.000	0.000	0.000	0.000	0.000
H4O9	0.000	0.000	0.000	0.000	0.000
H3C9	0.000	0.000	0.000	0.000	0.000
H4C9	0.000	0.000	0.000	0.000	0.000
MITC9*	0.054	0.031	0.010	0.015	0.022
MITC9is*	0.000	0.000	0.000	0.000	0.001

Table B.2: Relative error of displacements and strains in bending patch test.

Acronym key	Maximum error in w	Maximum error in θ_x	Maximum error in θ_y	Maximum error in κ_x	Maximum error in κ_y	Maximum error in κ_{xy}
H2O9	0.000	0.000	0.000	0.000	0.000	0.000
H3O9	0.000	0.000	0.000	0.000	0.000	0.000
H4O9	0.000	0.000	0.000	0.000	0.000	0.000
H3C9	0.000	0.000	0.000	0.000	0.000	0.000
H4C9	0.000	0.000	0.000	0.000	0.000	0.000
MITC9*	0.018	0.028	0.049	0.004	0.012	0.009
MITC9is*	0.000	0.000	0.000	0.000	0.000	0.000

Table B.3: Relative error of displacements and strains in membrane patch test (distorted mesh).

Acronym key	Maximum error in u	Maximum error in v	Maximum error in ε_x	Maximum error in ε_y	Maximum error in γ_{xy}
H2O9	0.000	0.000	0.000	0.000	0.000
H3O9	0.000	0.000	0.000	0.000	0.000
H4O9	0.000	0.000	0.000	0.000	0.000
H3C9	0.000	0.000	0.000	0.000	0.000
H4C9	0.000	0.000	0.000	0.000	0.000
MITC9*	0.212	0.112	0.040	0.435	0.210
MITC9is*	0.005	0.005	0.007	0.005	0.007

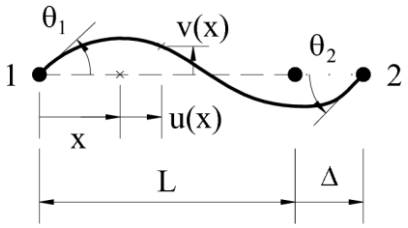

Figure 1: Configuration and deformation parameters for a local Euler-Bernoulli beam-column element.

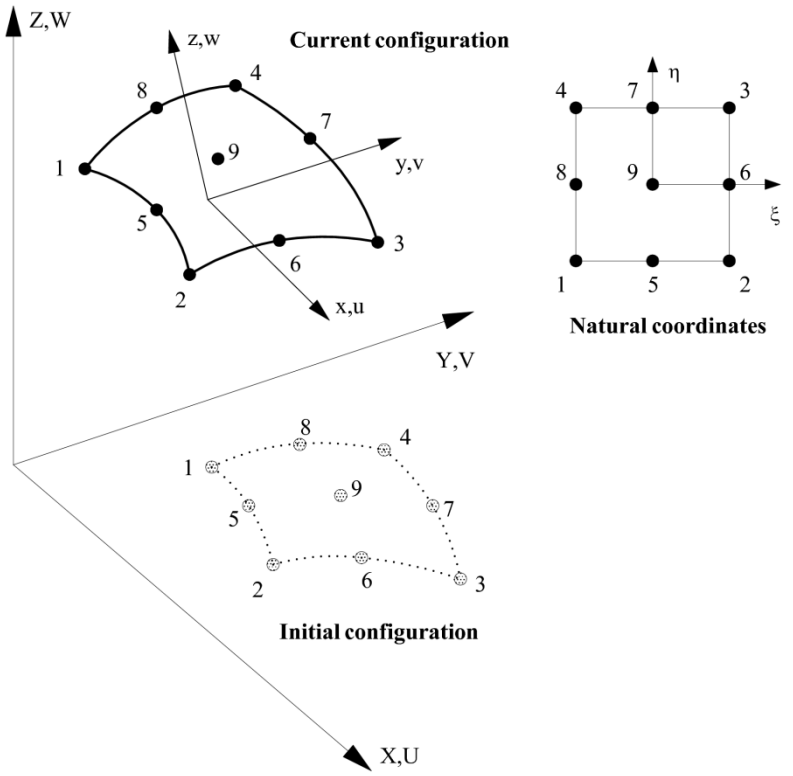

Figure 2: Global, local and natural coordinates for 9-noded shell element.

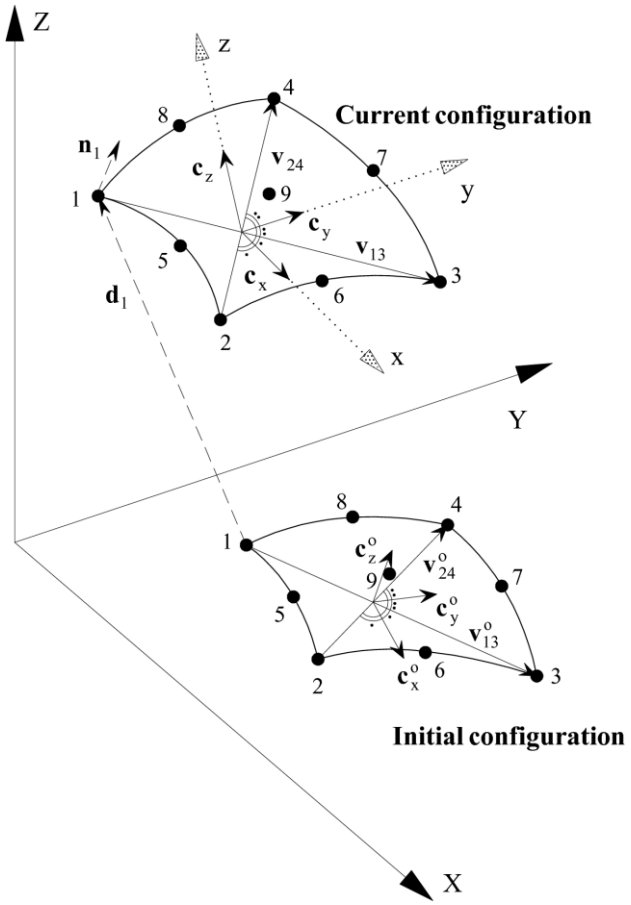

Figure 3: Bisector local coordinate system and global nodal parameters for 9-noded quadrilateral shell element.

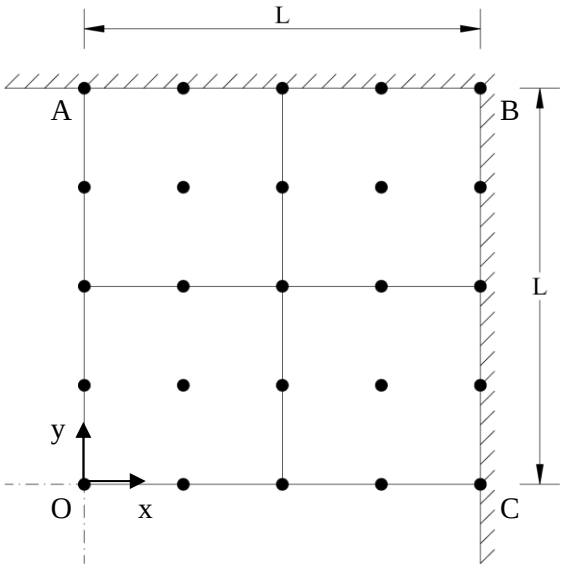

Figure 4: A quarter-model of a clamped square plate subjected to uniform pressure.

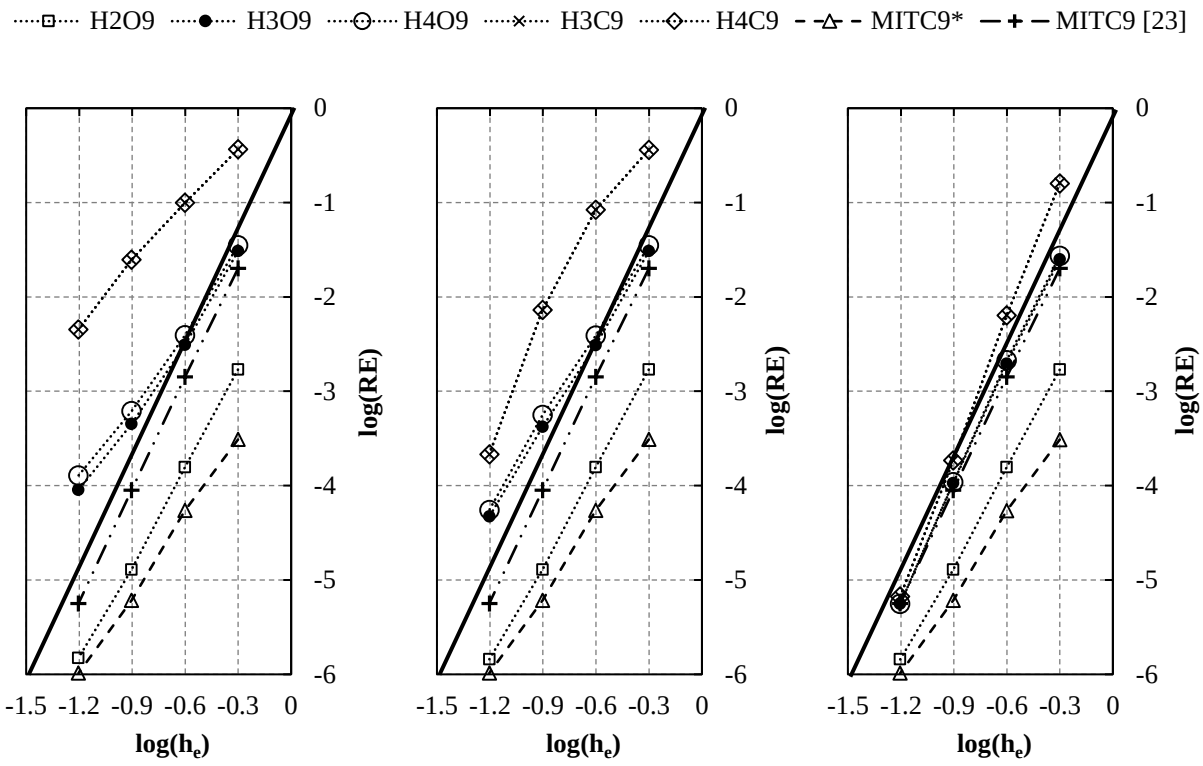

a. t/L = 0.0001 b. t/L = 0.001 c. t/L = 0.01

Figure 5: Convergence curves of various elements for the clamped square plate problem.

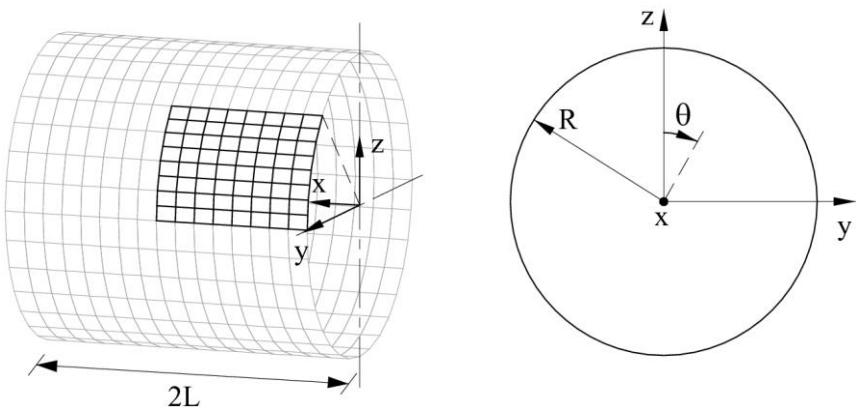

Figure 6: Cylindrical shell under periodical loading.

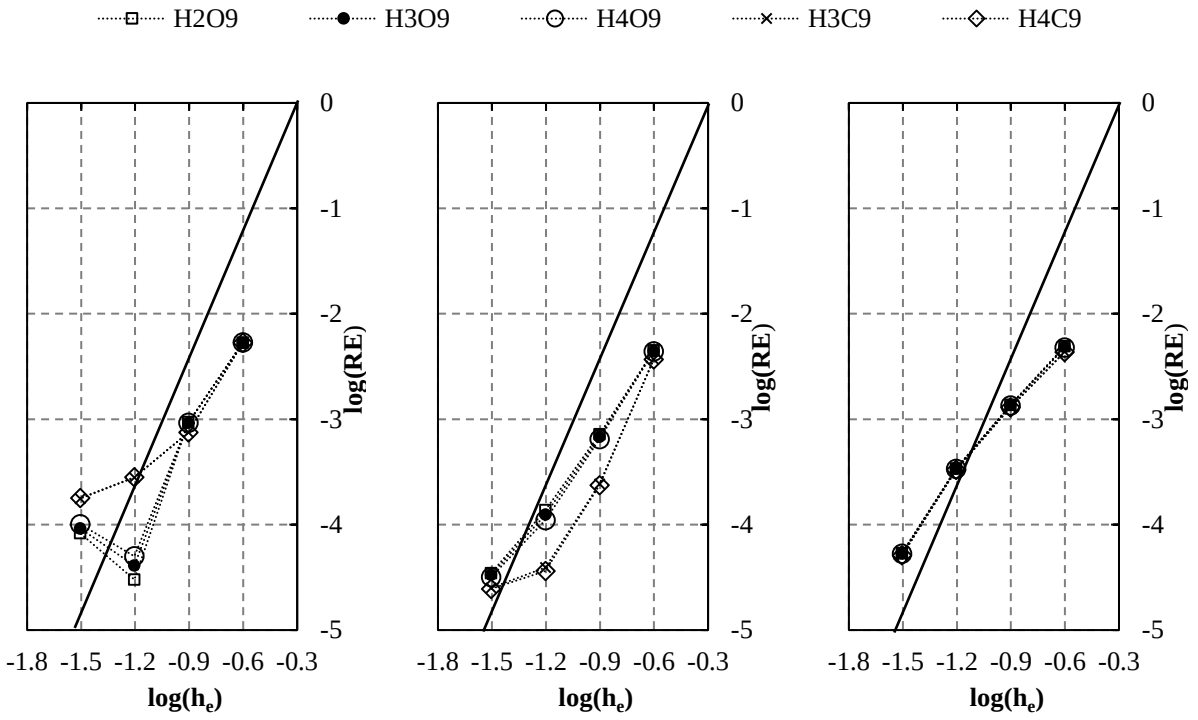

a. t/L = 0.0001 b. t/L = 0.001 c. t/L = 0.01

Figure 7: Convergence curves of various optimised elements for the cylindrical shell problem (free boundary).

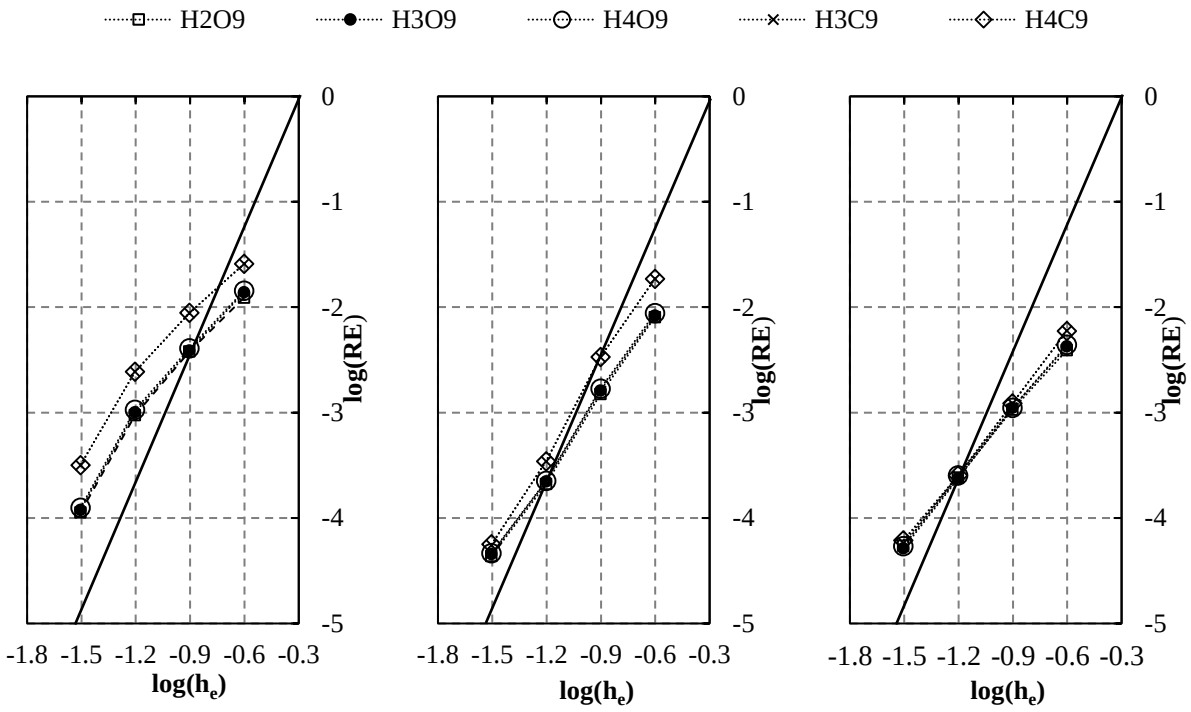

a. t/L = 0.0001 b. t/L = 0.001 c. t/L = 0.01

Figure 8: Convergence curves of various optimised elements for the cylindrical shell problem (clamped boundary).

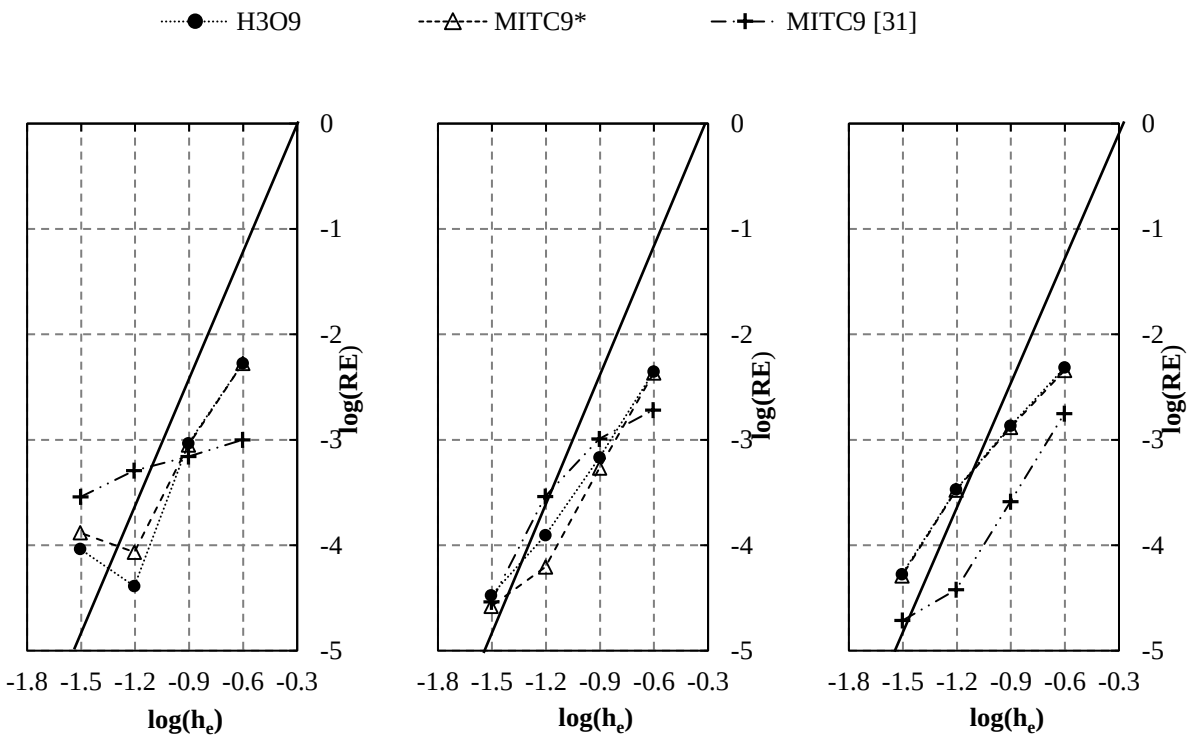

a. t/L = 0.0001 b. t/L = 0.001 c. t/L = 0.01

Figure 9: Convergence curves of H3O9, MITC9* and MITC9 elements for the cylindrical shell problem (free boundary).

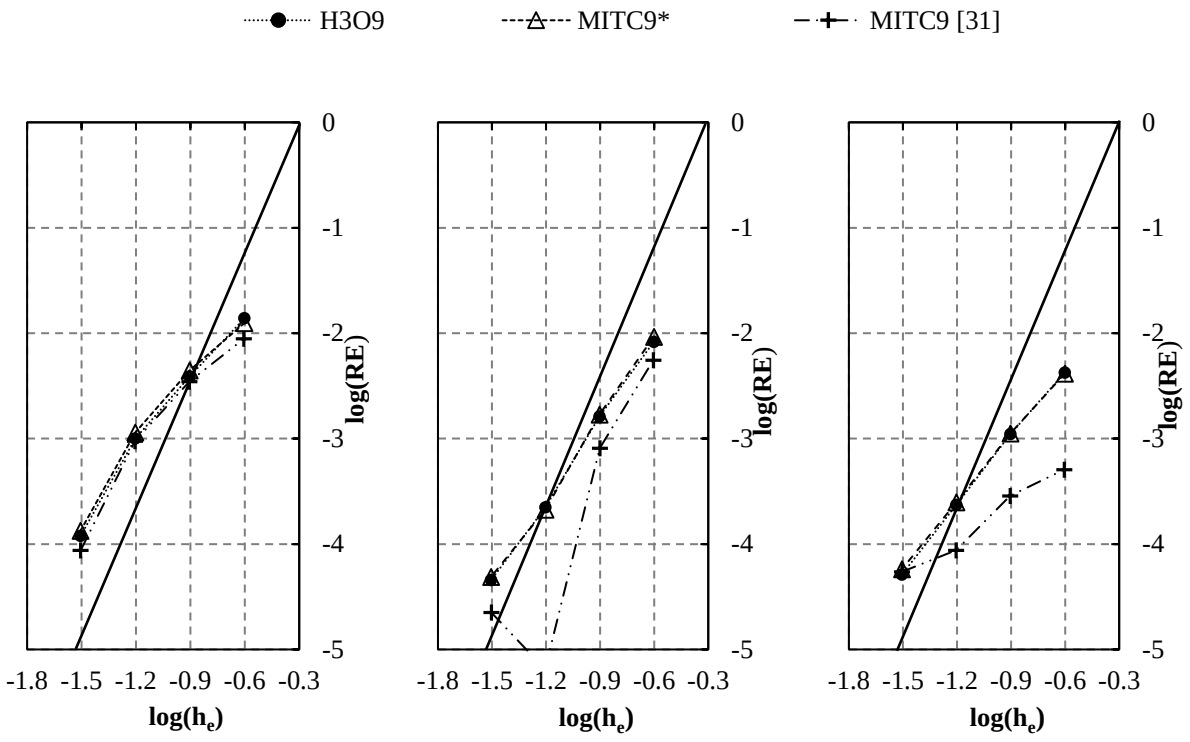

a. t/L = 0.0001 b. t/L = 0.001 c. t/L = 0.01

Figure 10: Convergence curves of H3O9, MITC9* and MITC9 elements for the cylindrical shell problem (clamped boundary).

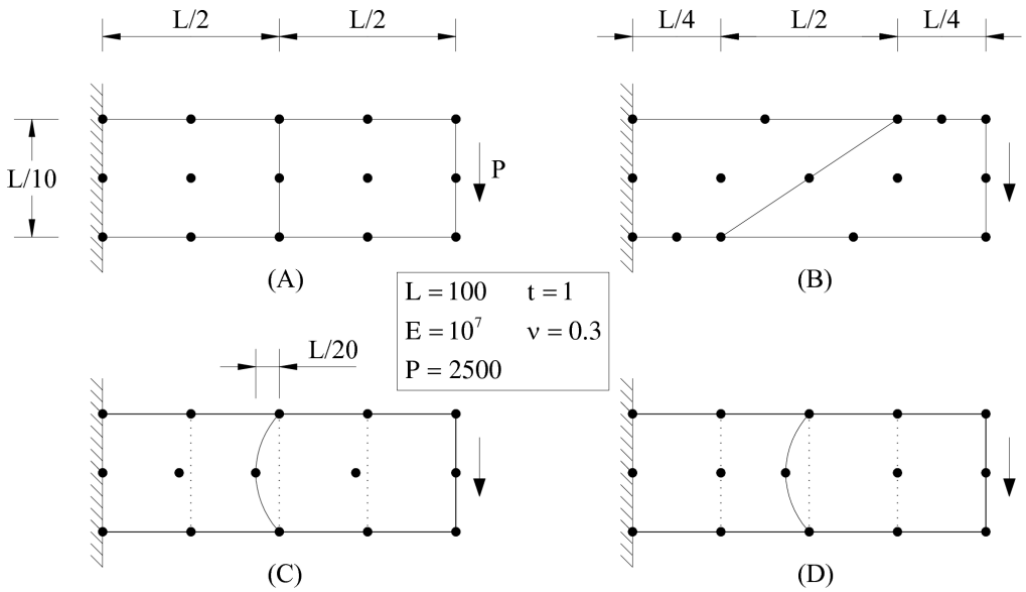

Figure 11: Cantilever modelled with different meshes using two 9-noded elements.

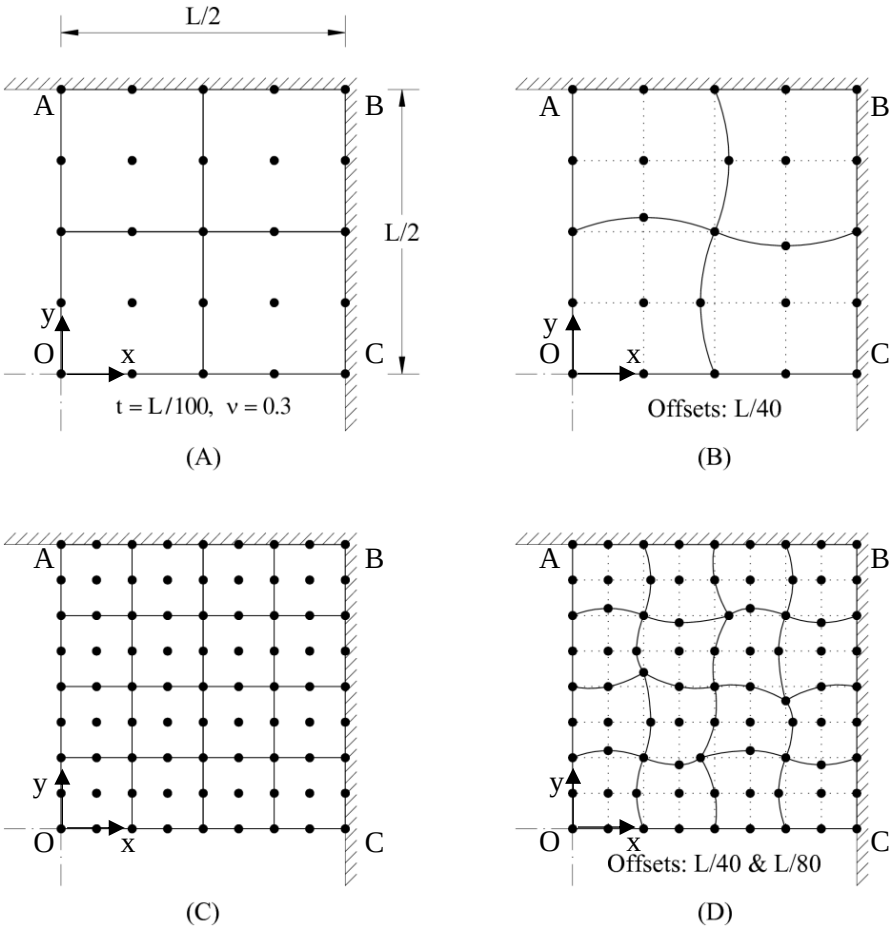

Figure 12: A quarter-model of a square plate using different mesh patterns of 9-noded elements.

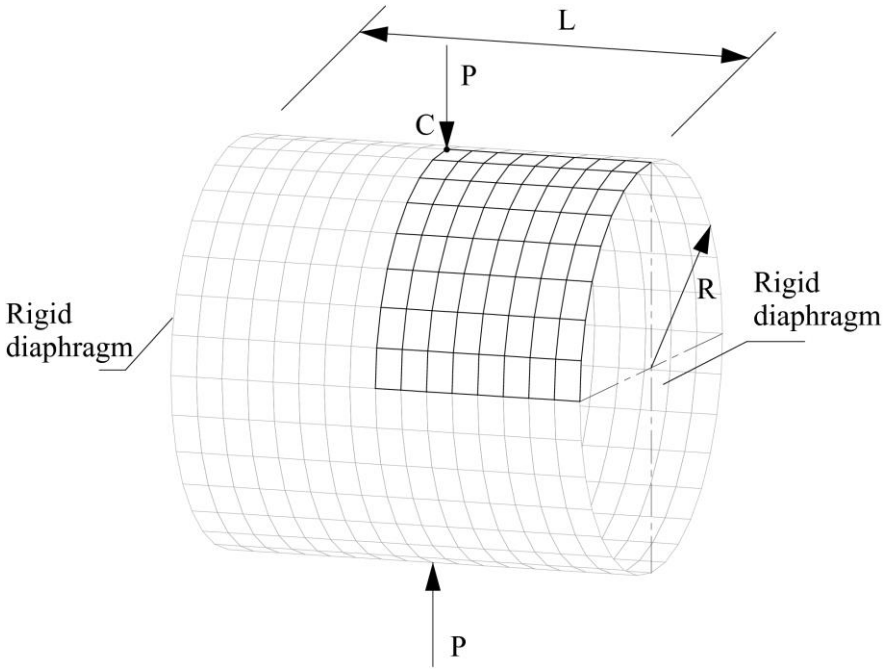

Figure 13: Pinched cylindrical shell supported by rigid diaphragms.

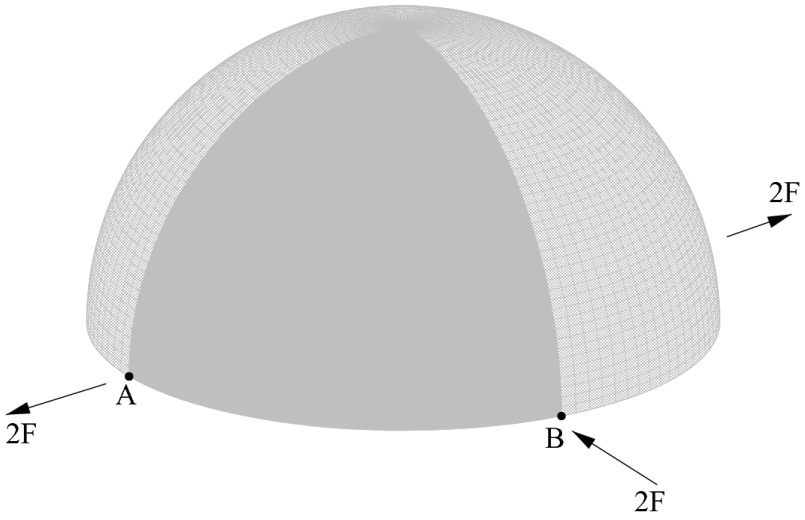

Figure 14: Pinched hemispherical shell.

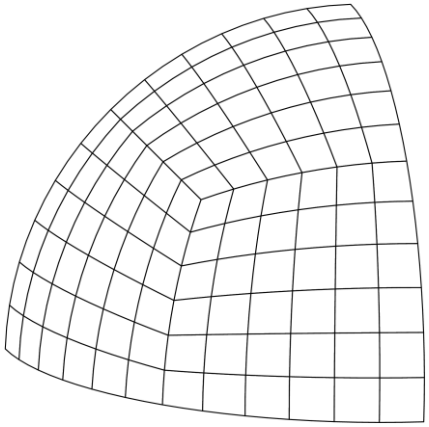

Figure 15: A 3×6×6 mesh of the quarter model.

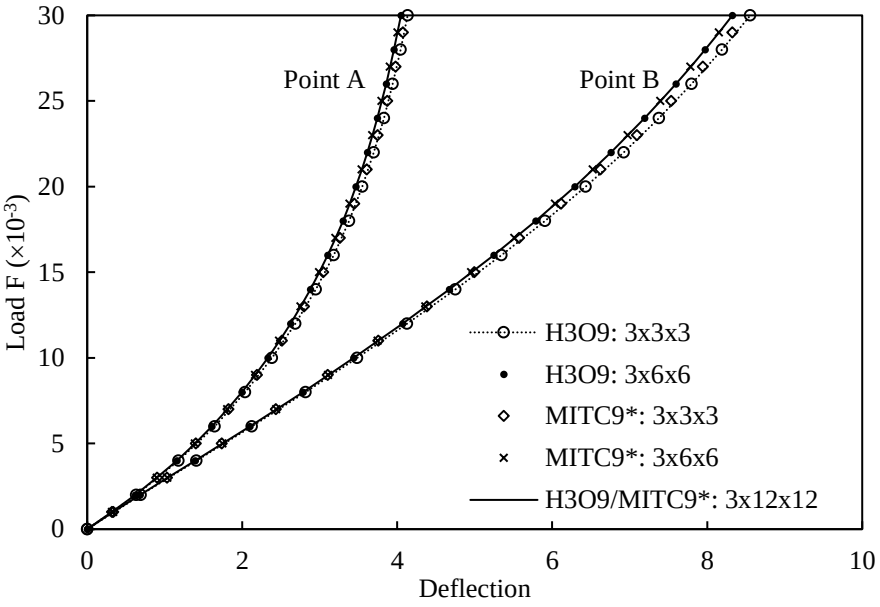

Figure 16: Convergence study of the hemispherical shell problem (t = 0.5).

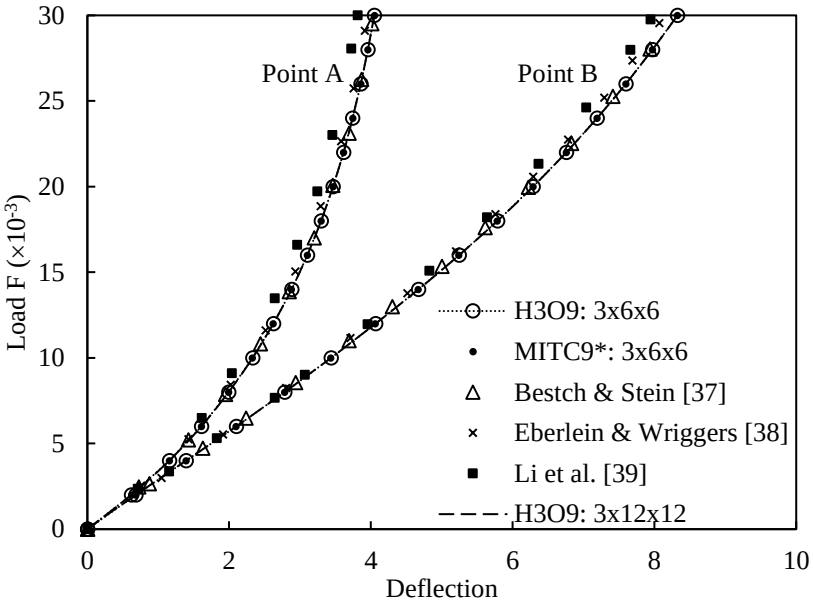

Figure 17: Comparison of load-deflection curves for the hemispherical shell problem (t = 0.5).

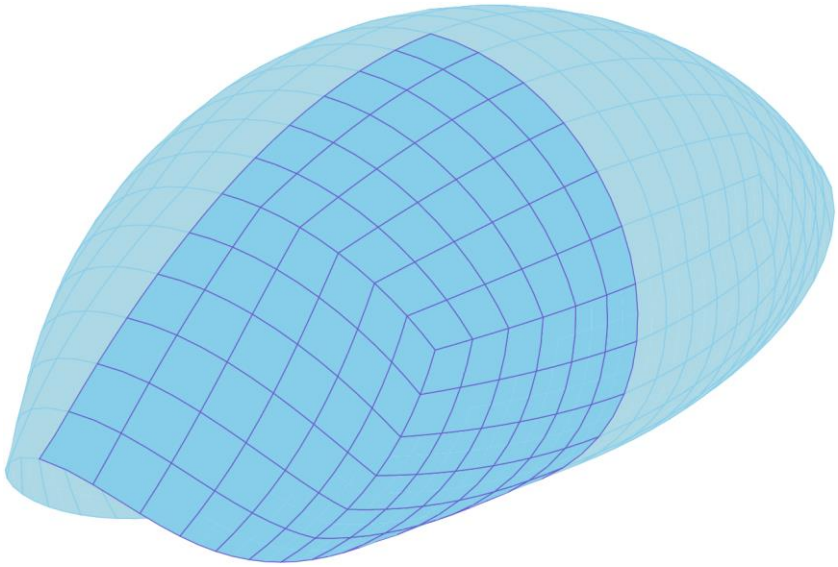

Figure 18: Deformed shape of the hemispherical shell ($F = 30\times10^{-3}$).

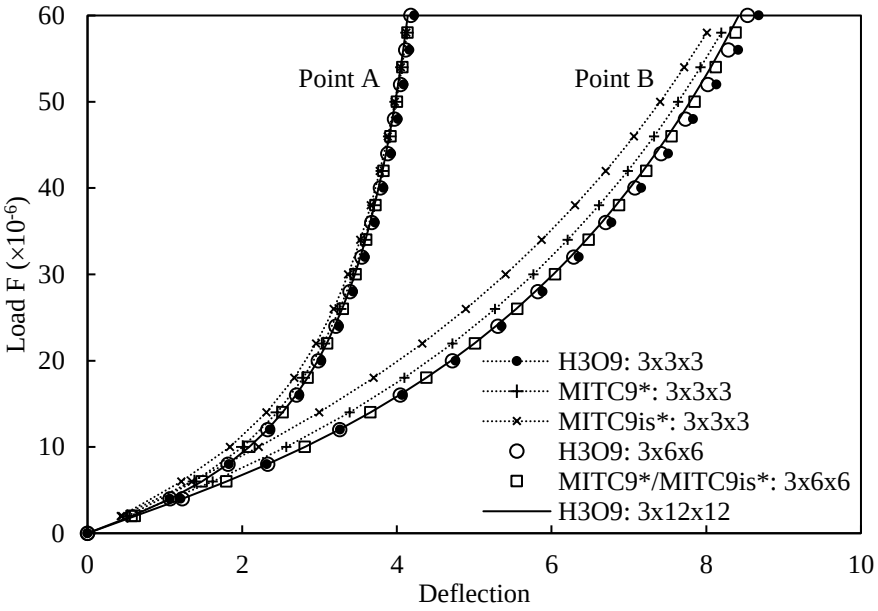

Figure 19: Convergence study of the hemispherical shell problem (t = 0.05).

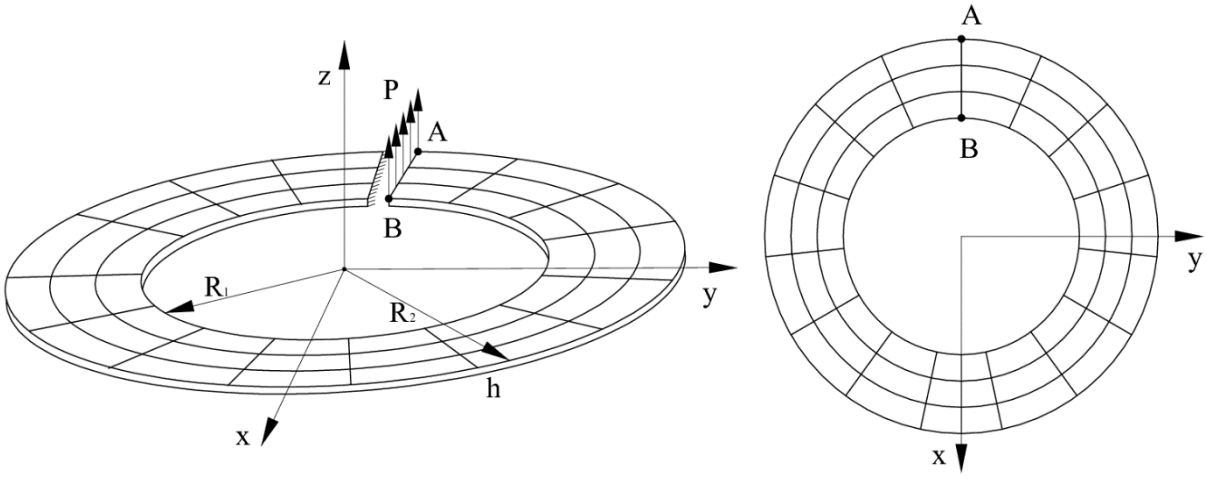

Figure 20: Annular plate subject to a uniform loading applied along the free edge.

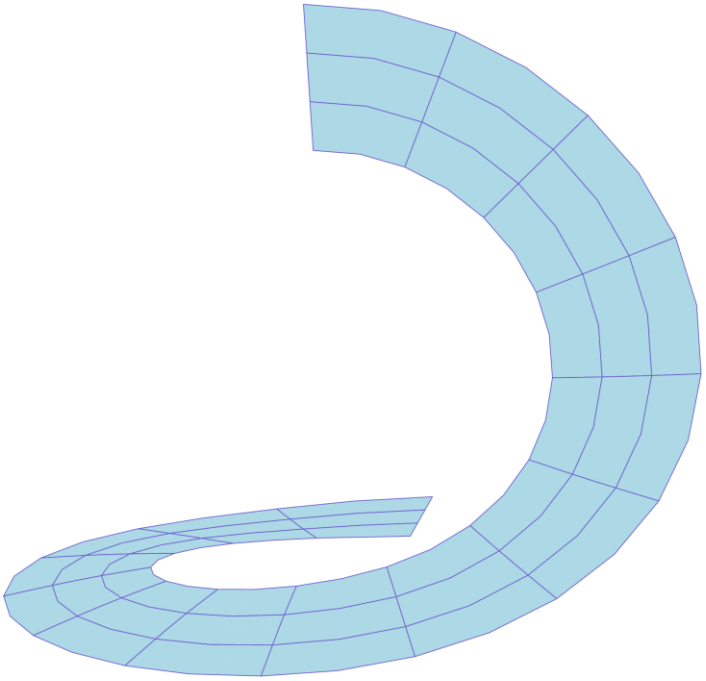

Figure 21: Deformed configuration of the annular plate problem ($p = 6$).

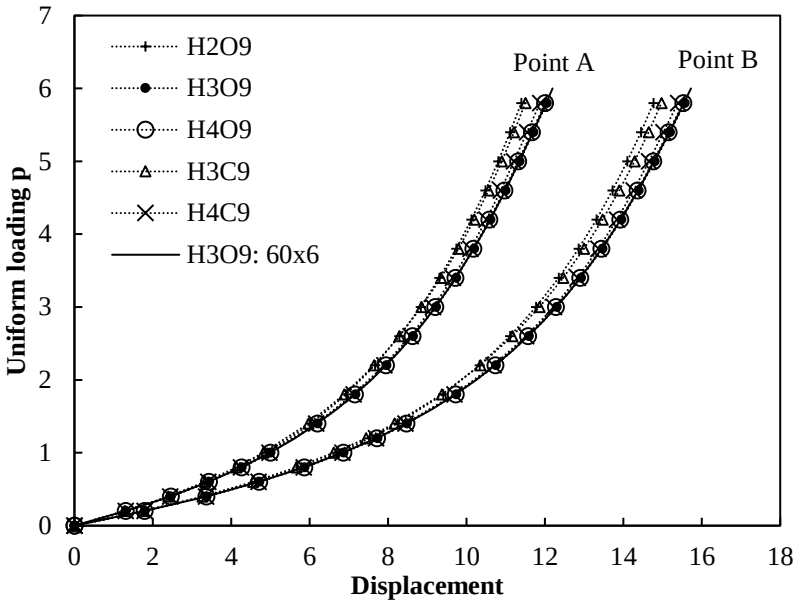

Figure 22: Load-displacement curves for a 15×3 mesh of various optimised elements.

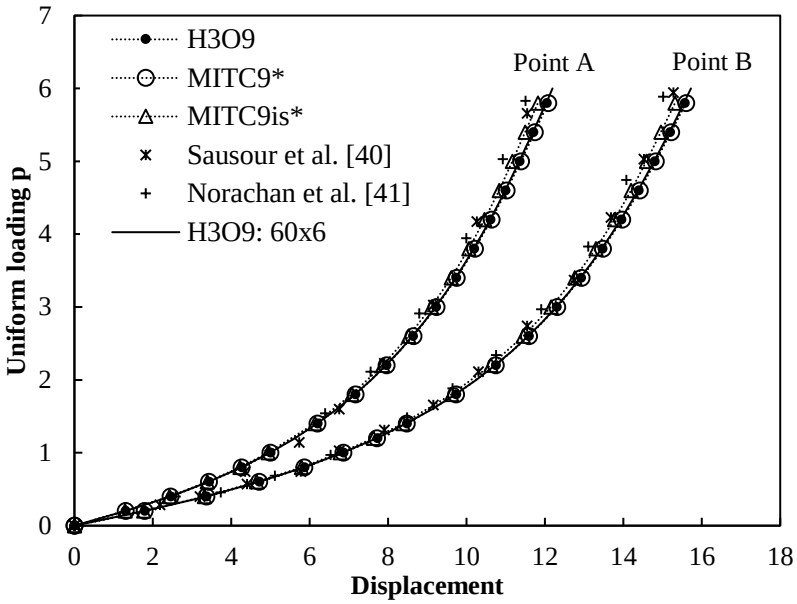

Figure 23: Load-displacement curves for meshes of various elements having the same number of DOFs.

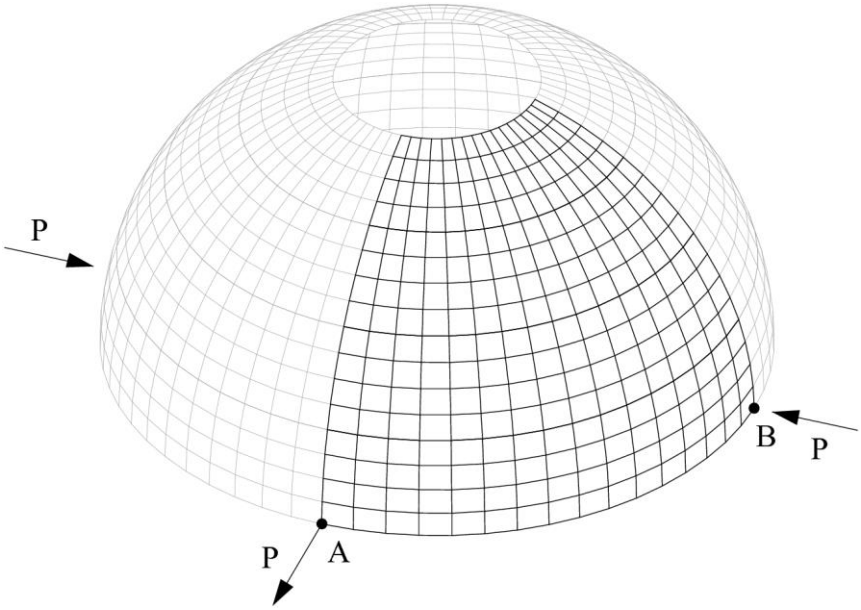

Figure 24: Pinched hemispherical shell with an 18° cut-off.

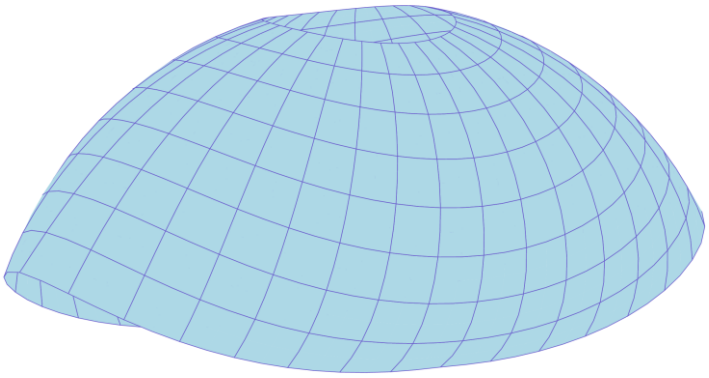

Figure 25: Deformed configuration of pinched hemispherical shell with an 18° cut-off (P = 320).

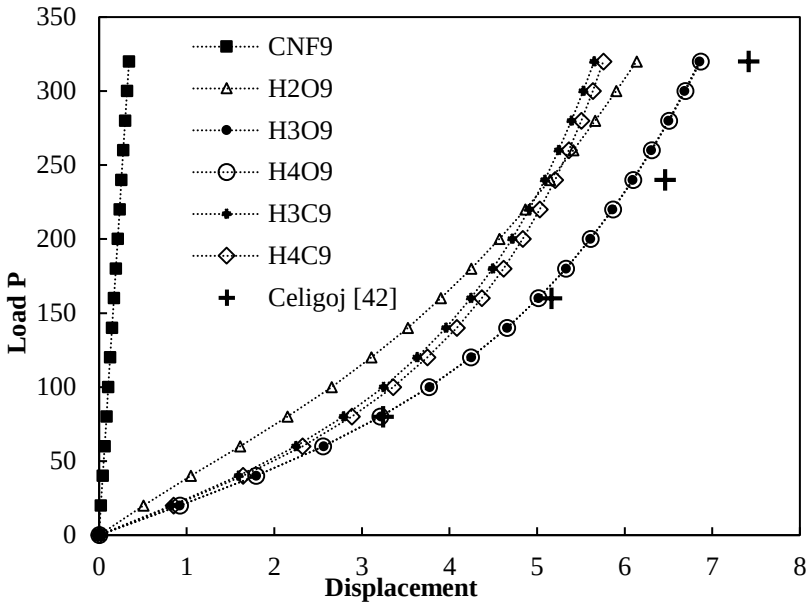

Figure 26: Load-displacement curves of the radial displacement at point B with different element types (4×4 mesh).

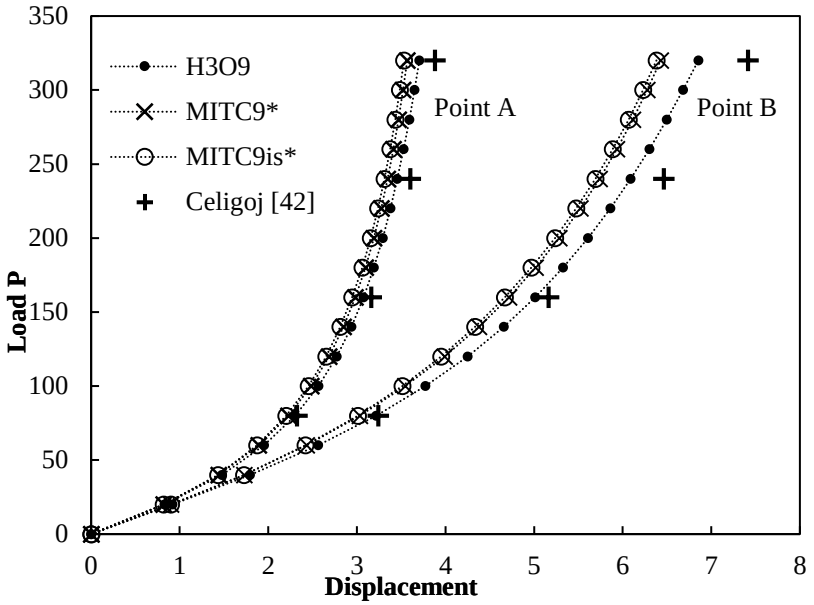

a. 4×4 mesh

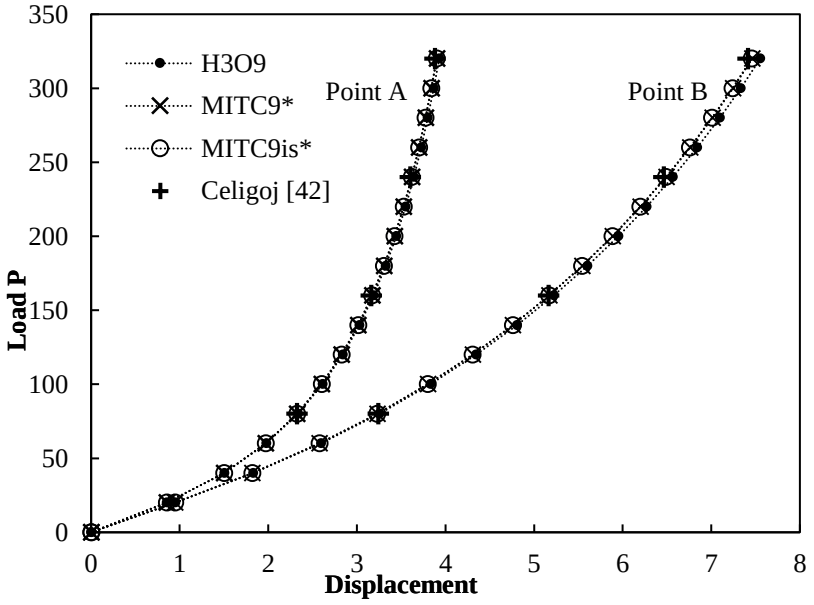

b. 8×8 mesh

Figure 27: Load-displacement curves of the radial displacements with different meshes (Cont'd…).

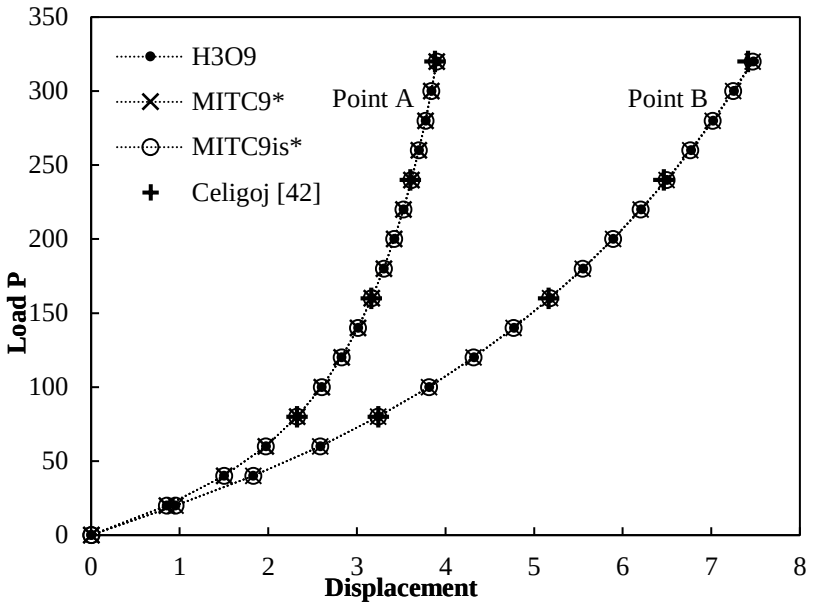

c. 16×16 mesh

Figure 27: Load-displacement curves of the radial displacements with different meshes.

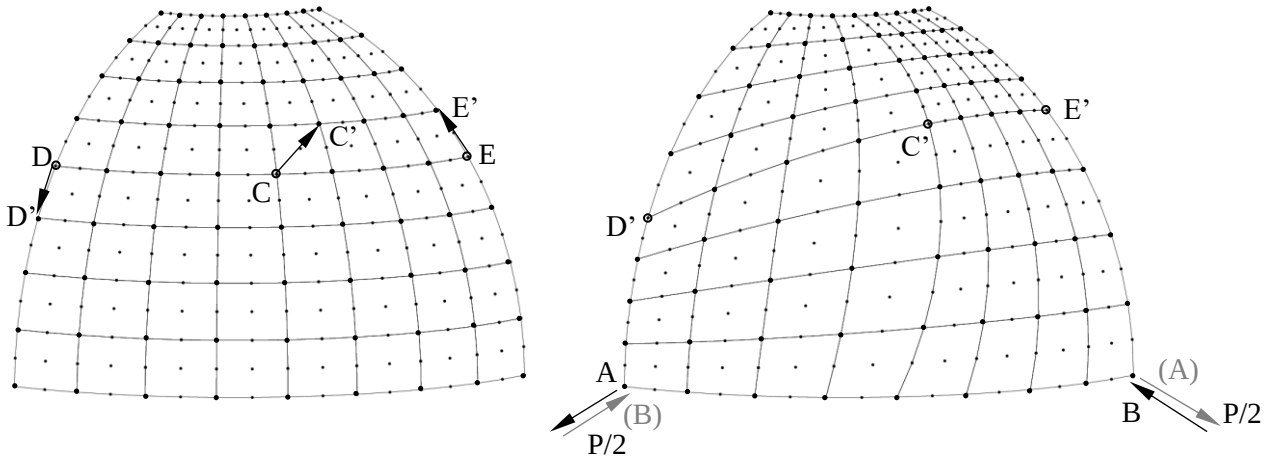

Figure 28: 8×8 irregular meshes of a quarter model. (Distorted mesh 1 corresponds to the inward and outward forces denoted in black, while Distorted mesh 2 corresponds to the forces denoted in grey.)

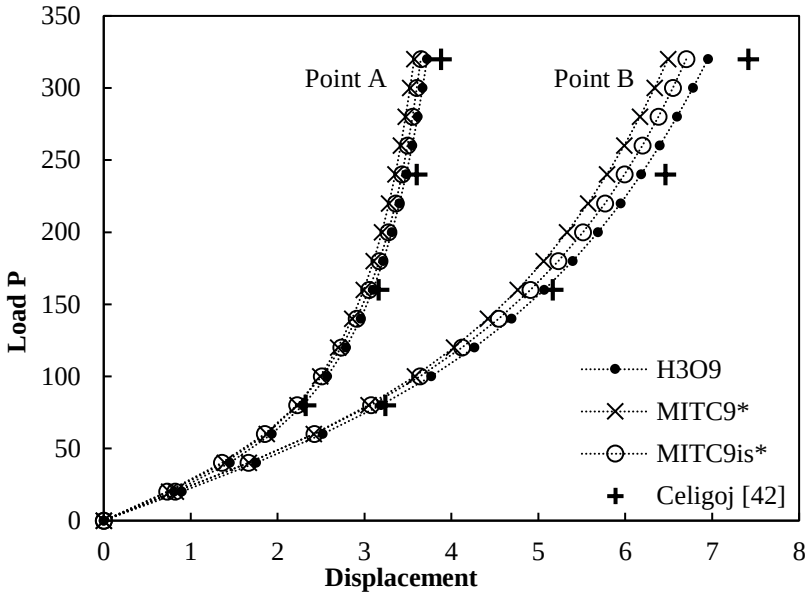

a. 4×4 mesh

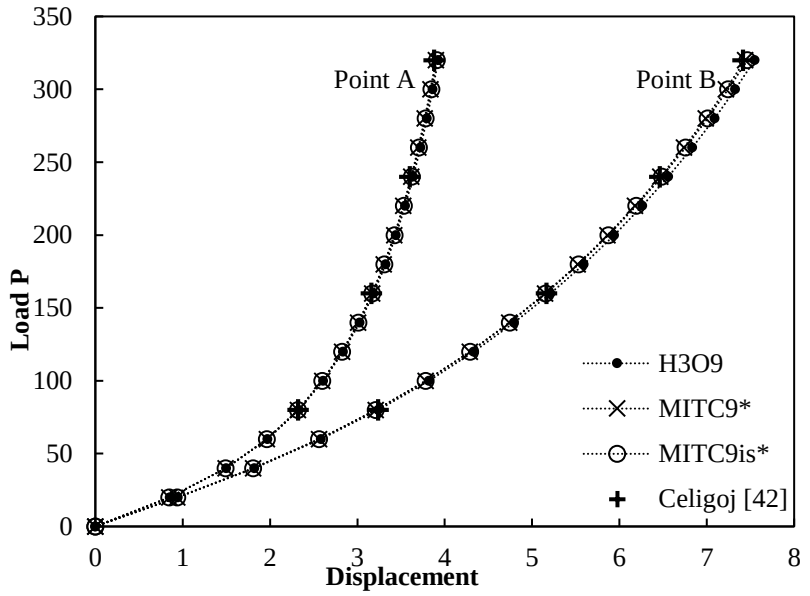

b. 8×8 mesh

Figure 29: Load-displacement curves for meshes of different elements (distorted mesh 1).

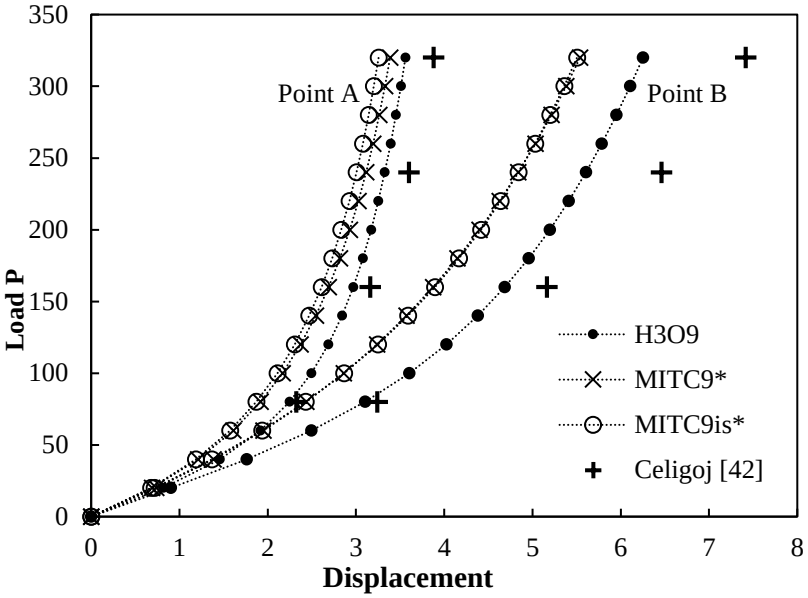

a. 4×4 mesh

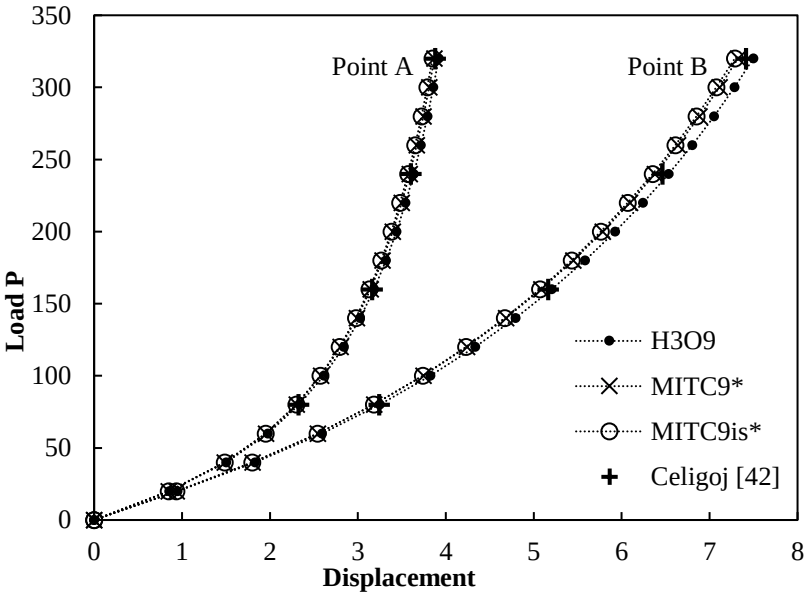

b. 8×8 mesh

Figure 30: Load-displacement curves for meshes of different elements (distorted mesh 2).

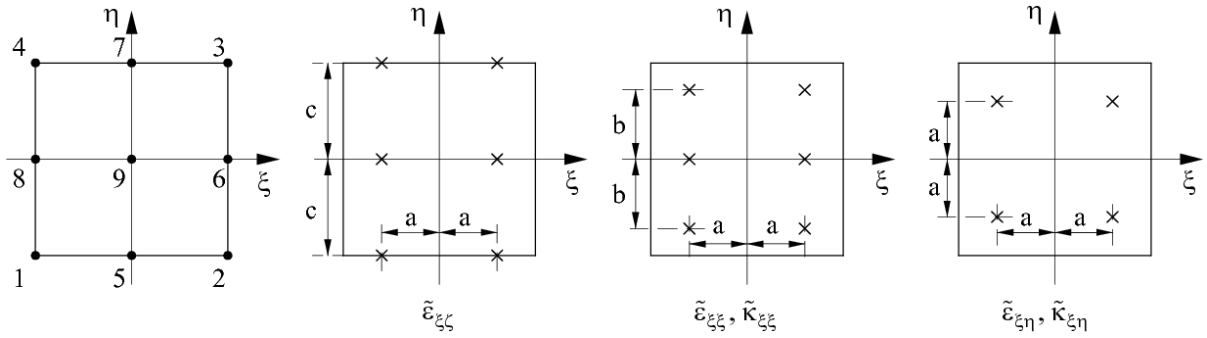

Figure A.1: Positions of tying points for MITC9 element [22] ($a = 1/\sqrt{3}$, $b = \sqrt{3/5}$, and $c = 1$).

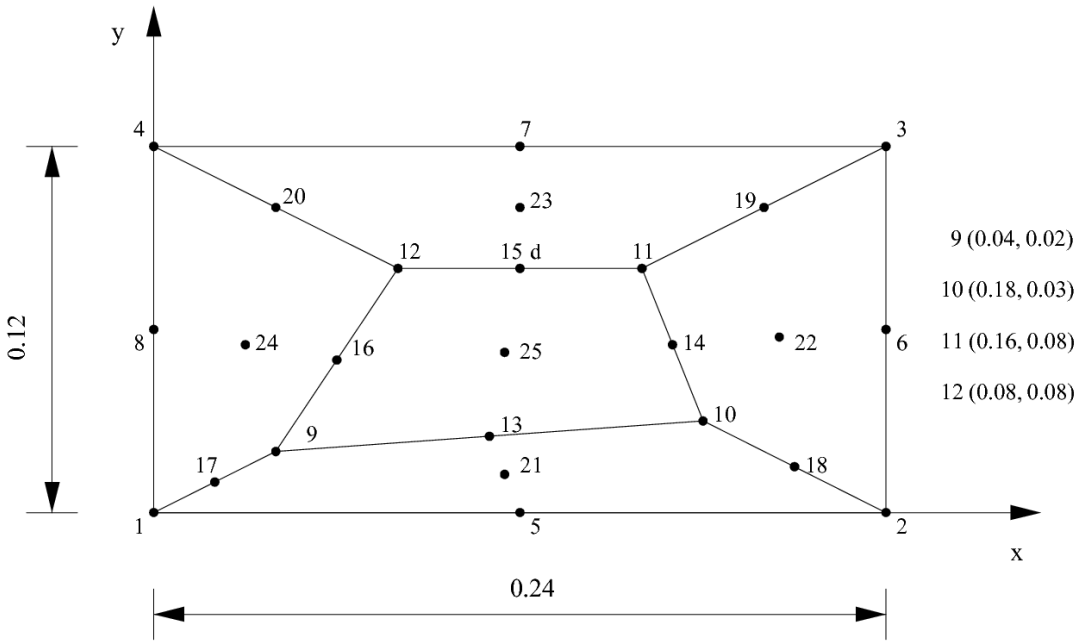

Figure B.1: Five-element patch test.

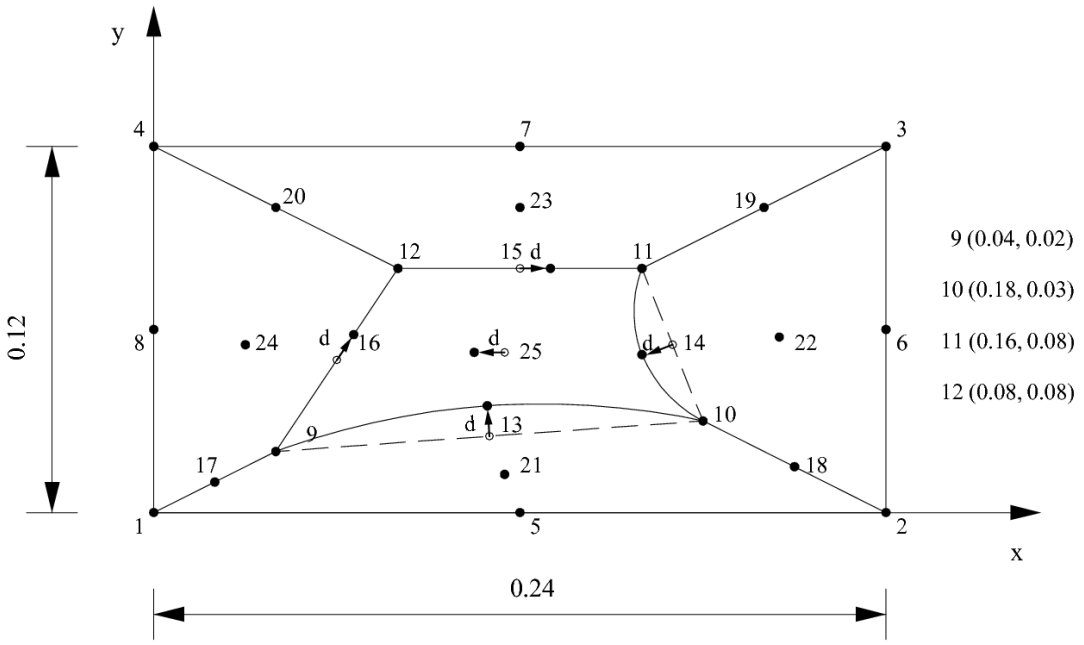

Figure B.2: Five-element patch test (distorted mesh).